



SANDIA REPORT

SAND2002-8567

Unlimited Release

Printed November 2002

Physical Basis for Interfacial Traction-Separation Models

N. R. Moody, E. D. Reedy, Jr., M. S. Kent

Prepared by
Sandia National Laboratories
Albuquerque, New Mexico 87185 and Livermore, California 94550

Sandia is a multiprogram laboratory operated by Sandia Corporation, a Lockheed Martin Company, for the United States Department of Energy under Contract DE-AC04-94AL85000.

Approved for public release; further dissemination unlimited.



Sandia National Laboratories

Issued by Sandia National Laboratories, operated for the United States Department of Energy by Sandia Corporation.

NOTICE: This report was prepared as an account of work sponsored by an agency of the United States Government. Neither the United States Government, nor any agency thereof, nor any of their employees, nor any of their contractors, subcontractors, or their employees, make any warranty, express or implied, or assume any legal liability or responsibility for the accuracy, completeness, or usefulness of any information, apparatus, product, or process disclosed, or represent that its use would not infringe privately owned rights. Reference herein to any specific commercial product, process, or service by trade name, trademark, manufacturer, or otherwise, does not necessarily constitute or imply its endorsement, recommendation, or favoring by the United States Government, any agency thereof, or any of their contractors or subcontractors. The views and opinions expressed herein do not necessarily state or reflect those of the United States Government, any agency thereof, or any of their contractors.

Printed in the United States of America. This report has been reproduced directly from the best available copy.

Available to DOE and DOE contractors from
U.S. Department of Energy
Office of Scientific and Technical Information
P.O. Box 62
Oak Ridge, TN 37831

Telephone: (865)576-8401
Facsimile: (865)576-5728
E-Mail: reports@adonis.osti.gov
Online ordering: <http://www.doe.gov/bridge>

Available to the public from
U.S. Department of Commerce
National Technical Information Service
5285 Port Royal Rd
Springfield, VA 22161

Telephone: (800)553-6847
Facsimile: (703)605-6900
E-Mail: orders@ntis.fedworld.gov
Online order: <http://www.ntis.gov/ordering.htm>



SAND2002-8567
Unlimited Release
Printed November 2002

Physical Basis for Interfacial Traction-Separation Models

N. R. Moody
Microsystems and Materials Mechanics-8725
Sandia National Laboratories
P.O. Box 969 MS9404
Livermore, CA 94551-0969

E. D. Reedy, Jr.
Material Mechanics-9123
Sandia National Laboratories
P. O. Box 5800
Albuquerque, NM 87185

M. S. Kent
Microsystems, Materials, Tribology and Technology-1851
Sandia National Laboratories
P.O. Box 5800
Albuquerque, NM 87185

Abstract

Many weapon components contain interfaces between dissimilar materials where cracks can initiate and cause failure. In recent years many researchers in the fracture community have adopted a cohesive zone model for simulating crack propagation (based upon traction-separation relations) Sandia is implementing this model in its ASCI codes. There is, however, one important obstacle to using a cohesive zone modeling approach. At the present time traction-separation relations are chosen in an ad hoc manner. The goal of the present work is to determine a physical basis for Traction-Separation (T-U) relations. This report presents results of a program aimed at determining the dependence of such relations on adhesive and bulk properties. The work focused on epoxy/solid interfaces, although the approach is applicable to a broad range of materials. Asymmetric double cantilevered beam and free surface film nanoindentation fracture toughness tests were used to generate a unique set of data spanning length scales, applied mode mixities, and yield (plastic) zone constraint. The crucial roles of crack tip plastic zone size and interfacial adhesion were defined by varying epoxy layer thickness and using coupling agents or special self-assembled monolayers in preparing the samples. The nature of the yield zone was probed in collaborative experiments run at the Advanced Photon Source. This work provides an understanding of the major phenomena governing polymer/solid interfacial fracture and identifies the essential features that must be incorporated in a T-U based cohesive zone failure model. We believe that models using physically based T-U relations provide a more accurate and widely applicable description of interface cracking than models using ad hoc relations. Furthermore, these T-U relations provide an essential tool for using models to tailor interface properties to meet design needs.

Table of Contents

I. Introduction	11
II. Experimental Work	14
II.1 Film Thickness Effects	14
II.1.1 Background	14
II.1.2 Materials and Procedure	14
II.1.2.1 Materials	14
II.1.2.2 Nanoindentation	15
II. 1.2.3 Fracture Mechanics Testing	15
II. 1.2.3.1 Asymmetric DCB	15
II.1.2.3.2 Nanoindentation	16
II.1.2.3.3 Stressed Overlayers and Nanoindentation	16
II.1.3 Results	17
II.1.3.1 Mechanical Properties	17
II.1.3.2 Asymmetric DCB Fracture	19
II.1.3.3 Thick Film Delamination	19
II.1.3.4 Thin Film Delamination	19
II.1.3.5 Interfacial Fracture Surface Analysis	22
II.1.4 Fracture Energy Analysis	25
II.1.4.1 Asymmetric DCB Fracture	25
II.1.4.2 Thick Film Indentation Delamination	25
II.1.4.3 Thin Film Telephone Cord Blister Formation	27
II.1.4.4 Thin Film Circular Blister Formation	31
II.1.4.5 Mode I Fracture Energies	35

II.1.4.6 Crack Tip Opening Angle Approach	39
II.1.5 Summary	40
II.2 Self Assembled Monolayers	42
II.2.1 Background	42
II.2.2 Materials and Procedure	43
II.2.2.1 SAM systems	43
II.2.2.2 Tensile Brazil Nut Samples	46
II.2.3 Fracture Energy Analysis	48
II.2.3.1 Surface Interactions	48
II.2.3.2 Bond Thickness	51
II.2.3.3 Mode Mixity	51
II.2.4 Summary	54
III Investigation of Crack Tip Structure Using X-rays	56
III.1 Background	56
III.2 Materials	56
III.3 Results	56
III.3.1 Polyethylene Studies	56
III.3.1.1 Background Work on Bulk Drawn Samples	57
III.3.1.2 Higher Resolution Studies on Notched Samples	57
III.3.2 Epoxy Studies	62
III.3.2.1 Small Angle X-ray Scattering	62
III.3.2.2 X-ray Tomography	62
III.4 Summary	65
IV. Interfacial Crack Growth Simulations	66

IV.1 Background	66
IV.2 Approach	66
IV.3 Model Inputs	68
IV.4 Crack Growth Simulations	69
IV.4.1 Small Scale Yielding	69
IV.4.1 Strain Energy Release Rate	72
IV.5 Summary	75
V. Acknowledgments	76
VI. Tables	77
VII. References	78

List of Figures

Figure II.1. Nanoindentation gave an (a) average near surface elastic modulus of 4.35 GPa and (b) an average hardness of 250 GPa for all films.

Figure II.2. The relationship derived by Marsh (1963) gives a strength of 115 MPa for the epoxy films of this study.

Figure II.3. The 11.8 μm thick epoxy film delaminated during indentation. The extent of delamination is clearly seen in this optical image.

Figure II.4. Stressed overlayers triggered extensive telephone cord blistering in the 24 nm thick epoxy film.

Figure II.5. (a) Indentation tests exhibited no excursion or discontinuity in the load versus displacement curve. The indentations triggered formation of (b) large circular blisters on the 164 nm thick epoxy film. (c) Atomic Force Microscopy of the blister further showed that material was not compressed into the film.

Figure II.6. Atomic Force Microscopy of the aluminum substrate surface, (a) top down and (b) 3-D profile views, showed no evidence of epoxy after testing. The average aluminum film grain size was 100 nm with an rms roughness of 7 nm.

Figure II.7. Delamination in the 11.8 μm thick film is modeled as an elastic disk under plane stress. Only radial and circumferential stresses are used in obtaining fracture energy. (Thouless, 1988; Ritter et al., 1989; Rosenfeld et al., 1990)

Figure II.8. Schematic showing model parameters used to determine transformed moment of inertia. (a) Bending and cross-section. (b) Equivalent moments. From Kriese et al., (1999).

Figure II.9. (a) Measurement location and (b) schematic of a telephone cord blister profile.

Figure II.10. (a) Fracture energies decreased with decreasing film thickness reaching a lower limiting value near 1.5 J/m². (b) Measured energies vary with blister morphology with the lowest values from circular blister measurements.

Figure II.11. (a) An AFM image of a circular blister and (b) a typical circular blister profile.

Figure II.12. (a) Schematic of blister cross-section showing moments and loads from which (b) phase angles of loading for circular and telephone cord (straightwall) blisters were calculated as a function of effective driving force. From Hutchinson and Suo (1992)

Figure II.13. (a) Mode I fracture energies decrease to a lower limiting value near 0.5 J/m^2 . (b) The mode I components of the measured fracture energies from telephone cord and circular blisters superimpose.

Figure II.14. (a) Measurement location and (b) crack tip opening angle (CTOA) across a telephone cord blister.

Figure II.15. Schematic showing (a) a mixed SAM along a substrate interface with (b) methyl and bromine terminated reactive groups.

Figure II.16. A one-to-one relationship exist between bromine in solution and bromine on the substrate surface.

Figure II.17. (a) A schematic depiction of the Tensile Brazil Nut Sandwich adhesively bonded sample used in this study.

Figure II.18. Variation of G_c with the % of bromine in the mixed monolayer SAM coating (interfacial interactions increase with the % bromine).

Figure II.19. Variation of G_c with bond thickness for a 50% bromine-terminated SAM coating.

Figure II.20. Variation of G_c with bond thickness for a 0% bromine-terminated SAM coating.

Figure II.21. Variation of the G_c of an epoxy/SAM-coated aluminum interface vs. applied mode mixity (75% bromine mixed monolayer SAM coating).

Figure III.1. X-ray diffraction data obtained for a bulk PE sample taken with a standard diffractometer at SNL. Draw ratios are: top curve - 9.45, middle curve - 1.0, and bottom curve - 0.0. The bottom figure is a blow-up of the higher q region where the martensitic transformation is evident. Incident radiation is 1.54 \AA .

Figure III.2. Small angle X-ray scattering data from the UNM SAXS lab on bulk, drawn samples of PE. The samples are the same as used in the diffraction study. The values in the legend are the extensions, corresponding to draw ratios of 0, 0.2, 0.98, 3.94, 6.30, 7.87, and 9.45.

Figure III.3. Notched PE sample showing the crack which has grown from the tip of the notch under loading.

Figure III.4. X-ray diffraction data obtained from the notched PE sample near the crack tip taken with a $300\ \mu\text{m} \times 300\ \mu\text{m}$ beam at the APS (without load). This same pattern was observed over the entire region around the crack tip as well as far away from the crack tip. However, the most sensitive region to the deformation occurs at higher q than obtained in this spectrum. Incident radiation is 17 KeV or $0.73\ \text{\AA}$.

Figure III.5. FE analysis of notched expoy sample. Deformation zone occurs ahead of the notch tip.

Figure III.6. High resolution computed X-ray tomography of the notched epoxy sample taken at the APS. The tip of the notch is at the right of the figure.

Figure IV.1. Traction-separation relation used to define the separation process in the interfacial crack growth simulations.

Figure IV.2. Compressive stress-strain relationship for the EPON 828/T-403 epoxy adhesive (solid curve) along with model used in calculations (dotted curve).

Figure IV.3. Finite element mesh used in the small-scale yielding crack growth simulations.

Figure IV.4. Convergence study to determine the minimum ratio of critical characteristic separation/element size needed to resolve cohesive zone ($\bar{\sigma}/\sigma_y=2.5$).

Figure IV.5. Calculated energy release rate to propagate an interfacial crack vs. crack extension as a function of $\bar{\sigma}/\sigma_y$.

I. Introduction

Interfacial cracking is a significant concern in many critical weapon applications. Polymer/solid interfaces are of special concern as this is where failure often initiates. For example, the Enhanced Surveillance Program needs to assess the likelihood that several bonded and potted components will operate reliably for one or more additional life cycles. However, the data generated by component level testing is often insufficient for assessing reliability and performance. This data must be augmented by high fidelity simulations that include interfacial separation. A vital aspect of the simulation effort is the development of failure models and the identification and measurement of the relevant fracture parameters. In recent years many members of the fracture community have adopted a cohesive zone model, based upon traction-separation relations, to simulate crack propagation. The two key parameters defining a Traction-Separation (T-U) relation are the work of separation (the area under the T-U curve) and the peak separation stress. The T-U approach appears particularly promising for several reasons. It is intuitively reasonable to characterize an interface by a force-separation law. It is well suited to computation. It reduces to classical Linear Elastic Fracture Mechanics for pure Mode I or Mode II loading in purely elastic materials. Moreover, this type of approach can potentially lead to mesh-independent results since a length scale is embedded within the T-U relationship.

There is, however, one important drawback to using a cohesive zone (i.e., T-U) modeling approach. At the present time interfacial traction-separation relations are chosen in an ad hoc manner. There is no rigorous theory for measuring and defining the T-U relationship for a polymer/solid interface. Toughness of a polymer/solid interface includes contributions from energy related processes involved in both the breaking of interfacial bonds and from dissipation within the fracture process and yield zones in the polymer surrounding the crack tip. Indeed, the energy dissipation in the polymer is typically orders of magnitude greater than that associated with breaking interfacial bonds. To develop physically accurate and quantitatively correct separation relationship, one must understand how fundamental phenomena, like interfacial adhesion and bulk yielding, affect the separation process.

Interfacial toughness characterizes when an existing interfacial crack will advance. It results from a complex combination of coupled processes that interact in a highly nonlinear manner. (Rice, 1988; Hutchinson and Suo, 1992). While adhesion defines the separation stress, the energy dissipated within the polymer by crack tip deformation is often the primary contributor to interfacial toughness. A portion of this dissipation can be associated with intense non-homogeneous deformation within the fracture process zone (e.g., voids and shear banding). In many cases homogeneous yielding, either localized at the crack tip (small-scale yielding) or in other instances influenced by external boundaries (large-scale yielding), is the most significant source of dissipation. One aspect of interfacial fracture mechanics that distinguishes it from traditional linear elastic fracture mechanics is the role of mode mixity. Crack-tip mode mixity is a measure of the relative amount of shear deformation and has a huge effect on measured interfacial toughness. The larger the crack-tip shear deformation, the larger the yield zone and the greater the toughness. Mode mixity is influenced by elastic mismatch, and will change with specimen geometry and loading. However, to progress beyond ad hoc solutions, it is imperative to distill the essence of these coupled phenomena within the context of a T-U relation.

Our approach was to make a thorough evaluation of the effects of yielding and adhesion since these are the primary factors controlling interfacial toughness. Both sandwiched-layered beam as well as free-surface film nanoindentation fracture toughness tests were used to generate a unique set of data spanning length scales, applied mode mixities, and constraint on the plastic yield zone. Yield zone constraint was examined by changing the epoxy layer thickness over the range from 24 nm to 500 μm , while adhesion between the substrate and an epoxy layer was varied using special self-assembled monolayers (SAMs). Measurements on different length scales with differing degrees of adhesion and constraint were then used to define the role of crack-tip yielding. In addition to toughness measurements, direct measurements were initiated to characterize structural evolution of the polymer/solid crack-tip region in collaborative experiments conducted at the Advanced Photon Source.

The results of this work are described in the following sections of this report. Section II presents experimental results and comprises the bulk of the

work. It is divided into sub-sections on film thickness and self assembled monolayers. The sub-section on thickness addresses the effects of yielding and constraint on interfacial fracture toughness. The subsection on self-assembled monolayers addresses the effects of adhesion of interfacial toughness. Section III describes the use of x-ray scattering and imaging techniques to study the evolution of structure near crack tips. The results strongly suggest that mapping strain fields near crack tips is possible and can provide insight into crack initiation processes. Section IV describes a preliminary attempt to develop a T-U based simulation of crack growth along a polymer/solid interface that is consistent with our experimental results. The summary of results presented in Section IV shows that the comprehensive set of experimental results allowed us to identify the essential inputs that must be incorporated in a T-U based cohesive zone failure model that provides an accurate and widely applicable description of interface cracking.

II. Experimental Work

II.1 Film Thickness Effects

II.1.1 Background

Adhesion is an important factor in controlling the reliability of thin polymer films on metal substrates. However, our understanding of failure in these systems is limited by a lack of established test techniques for very thin layer systems. Traditional test techniques such as double cantilever beam sandwich samples (Kent et al., 2000) often require relatively thick films while peel tests are dominated by plastic energy contributions as the film is bent. (Wei and Hutchinson, 1998) In addition, it is difficult to maintain uniform film thickness in traditional sandwich geometries when bonds are less than one micron thick. The work of Bagchi et al. (1994, 1996), and more recently the work by Kriese and coworkers (1998, 1999) and Zhuk et al. (1998) shows that these limitations can be overcome for testing thin metal and polymer films by deposition of a relatively hard highly stressed overlayer. In this portion of the program, we used asymmetric double cantilever beam sandwich samples and combined stressed overlayers with nanoindentation to study the effect of film thickness on the interfacial fracture of thin epoxy films on aluminum substrates.

II.1.2 Materials and Procedure

II.1.2.1 Materials

Epon 828/T403 was chosen for study as the mechanical properties and structure are well characterized. (Kent et al., 2000) It consists of a 100:43 ratio of Epon 828 resin and T403 hardener. Aluminum asymmetric double cantilever beam sandwich (ADCBS) samples and thin epoxy films on aluminized glass substrates were used as these systems complement applications.

The ADCBS specimen (Akisanya and Fleck 1992) used in this study was fabricated by bonding together 4.6 and 9.4 mm thick beams (both beams are 12.7-mm deep and 120-mm long) with a thin epoxy layer and given a 50°C/2-5 day cure. The epoxy's glass transition temperature was ~70°C (DMA measured onset

of rubbery response). Each ADCBS specimen was fabricated separately. Small spacers were bonded to the ends of the thicker adherend to define the epoxy layer thickness, and the thinner adherend was subsequently positioned on top. Teflon tape was then applied to the edges of the specimen to contain the epoxy resin. The thin film samples were created by sputter depositing 200 nm of aluminum onto microscope glass slides to create the sample substrates. These substrates were plasma-cleaned and spin-coated with Epon 828/T403 to thicknesses of 24, 164, 615, and 11800 nm and given a 50°C/5 day cure.

II.1.2.2 Nanoindentation

The elastic modulus and hardness values of the films were measured using the continuous stiffness measurement option on a Nano Indenter II™ with a Berkovich diamond indenter at a superimposed excitation frequency of 45 Hz and displacement of 3 nm. (Lucas et al., 1998a, 1998b) An approach rate of 2 nm/s was used to minimize kinetic effects and surface contact was defined by the point of deviation in the phase angle versus displacement curve. Ten indentations were made on each sample. All tests were conducted in air at 22°C, well below the glass transition temperature of 68°C. The mechanical property test procedure used in this study was developed in a concurrent LDRD. (Emerson et al. 2002)

II. 1.2.3 Fracture Mechanics Testing

II. 1.2.3.1 Asymmetric DCB

Interfacial fracture toughness was first measured for an 828/T403 epoxy on aluminum Asymmetric Double Cantilevered Beam Sandwich samples. The specimen is loaded by means of a load train that utilizes a chain linkage and is loaded by pulling the ends apart at a crosshead displacement rate of 0.02 mm/s to propagate a crack along the interface with the thinner beam. The crack grows stably with increasing end displacement allowing several critical strain energy

release rates for fracture (fracture energy), G_c , to be made while testing a single specimen. G_c depends on the load to propagate a previously arrested crack and the associated crack length (inferred from the measured specimen compliance). The calibration used to determine G_c from the measured load and crack length is based upon results for a single material DCB (Bao, et al., 1992). A detailed finite element analysis of the specimen that explicitly modeled a 1-mm thick bond indicates that the G values determined with this calibration are within 3% of the calculated results for the ADCBS specimen. The finite element analysis also indicates that this specimen has a mode mixity of $y_{r=0.01\text{ mm}}$ of -8° .

II.1.2.3.2 Nanoindentation

Nanoindentation was used to induce fracture in the 11.8 μm thick film. The indentation fracture tests were run using a conical diamond tip with an 8.3 μm tip radius on the Nano Indenter IITM test system used to measure thin film properties. Loads were applied at a rate of 300 $\mu\text{N/s}$ to a predetermined depth, held for five minutes, and then removed. Indentations were arranged in a rectangular array and ranged in depth from 2 to 16 μm . The indentations were studied using optical microscopy with Nemarski contrast, a field emission gun scanning electron microscope, and an atomic force microscope. The regular arrays facilitated locating and observing the indentations.

II.1.2.3.3 Stressed Overlayers and Nanoindentation

Additional stress from tungsten overlayers was required for testing thinner films. Tungsten overlayer deposition was accomplished by placing the epoxy films into a sputter deposition chamber, evacuating to 3×10^{-6} torr, backfilling with 2.5 mtorr argon gas, and sputter depositing tungsten at a rate of 0.2 nm/s to a final thickness of 220 nm. A companion silica wafer showed that deposition induced a compressive residual stress in the tungsten films of -2.2 GPa. Following deposition, indentation fracture tests were conducted using the

Nano Indenter II™ with a 1 μm radius conical diamond tip. All indentations were examined optically and several were examined using atomic force microscopy (AFM).

II.1.3 Results

II.1.3.1 Mechanical Properties

Elastic modulus and hardness were obtained as a function of depth for each film as shown in Figure II.1. These data show that elastic modulus and hardness reach a plateau near the surface and maintain these values into the film before substrate effects begin to affect the measurements. The plateaus give an average near surface modulus of 4.35 GPa and hardness for all films of 250 MPa. From these values a yield strength of 115 MPa was estimated for all films using the following the empirical relationship between hardness and yield strength of glasses and glassy polymers derived by Marsh (1963).

$$H/\sigma_{ys} = C + K \ln(Z) \quad (1)$$

In this expression

$$\begin{aligned} \nu &= (1-2\nu)/\sigma_{ys} / E \\ \nu &= (1+\nu)\sigma_{ys} / E \\ B &= 3/(3-\nu) \\ Z &= 3/(\nu+3\nu-\nu\nu) \end{aligned} \quad (2)$$

$C=0.28$, and $\nu=0.6$. With E set to 4.35 GPa and $\nu = 0.38$, equation (1) gives a yield strength for the film of 115 MPa. (Figure II.2) These values are slightly higher than the elastic modulus of 3.5 GPa and yield strength of 90 MPa measured using compression tests on bulk samples. (Kent et al., 2000)

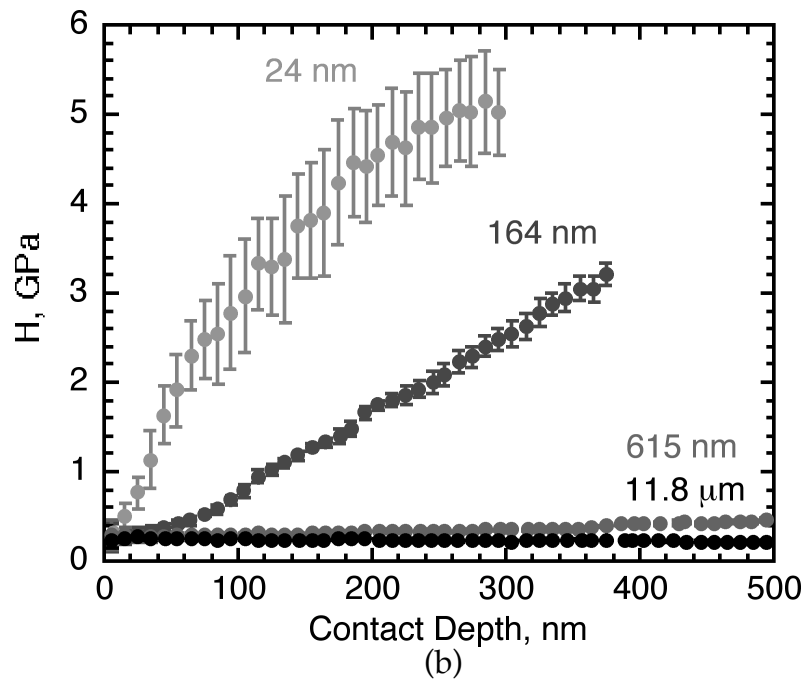
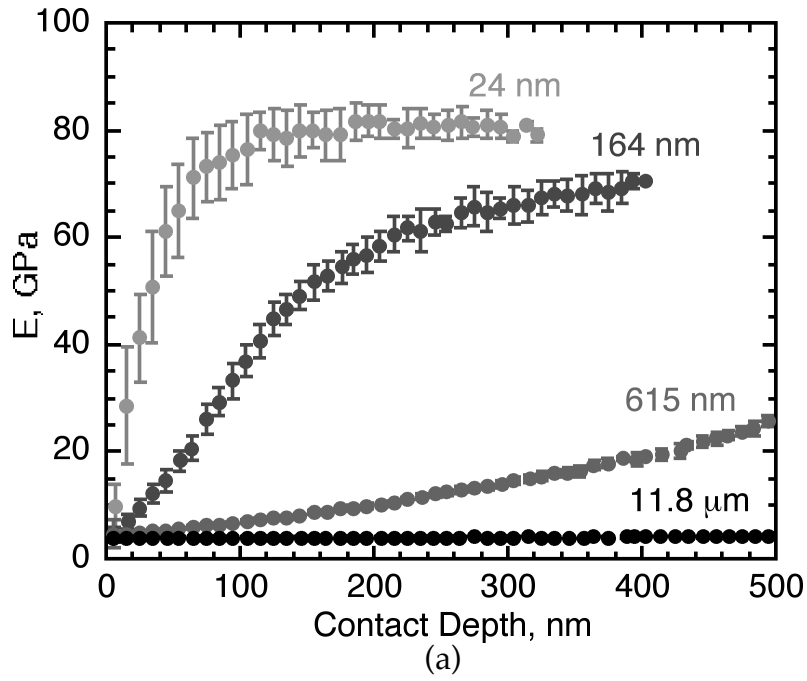


Figure II.1. Nanoindentation gave an (a) average near surface elastic modulus of 4.35 GPa and (b) an average hardness of 250 GPa for all films.

II.1.3.2 Asymmetric DCB Fracture

The measurement was made with an ADCBS specimen with a 0.5-mm thick bond. A visual examination of the failed specimen revealed that the crack runs along the interface and there is no indication of cohesive failure.

II.1.3.3 Thick Film Delamination

During the indentation fracture tests on the 11.8 μm thick epoxy film, interfacial delamination occurred as the indenter approached the substrate. This mode of fracture is shown in Figure II.3. Comparing optical images and corresponding load-displacement traces confirmed that delamination occurred at depths of penetration close to the film thickness. The optical images also provided interfacial crack diameters. (Strojny et al., 2000) However, the stresses triggering delamination were not sufficient to drive blister formation. It should be noted that the conical shape to the delaminated regions is due to adhesion of the film to the diamond indenter as the indenter is withdrawn from the sample at the end of each test.

II.1.3.4 Thin Film Delamination

Energies sufficient to trigger delamination could not be generated by indentation in the thinner films. This necessitated using overlayers to uniformly stress these films. Following the work of Bagchi and Evans (1994), Bagchi et al. (1996), Kriese and coworkers (1998, 1999) and Zhuk et al. (1998), highly stressed overlayers of tungsten were deposited onto the thin films. The deposition process was developed using the 24 nm thick Epon 828/T403 films in a companion LDRD and then applied to all films of this study. (Emerson et al., 2003) Deposition of the tungsten overlayers triggered extensive interface delamination and telephone cord blistering in the 24 nm thick film. (Figure II.4) There was also some spontaneous telephone cord blistering on the 164 nm thick

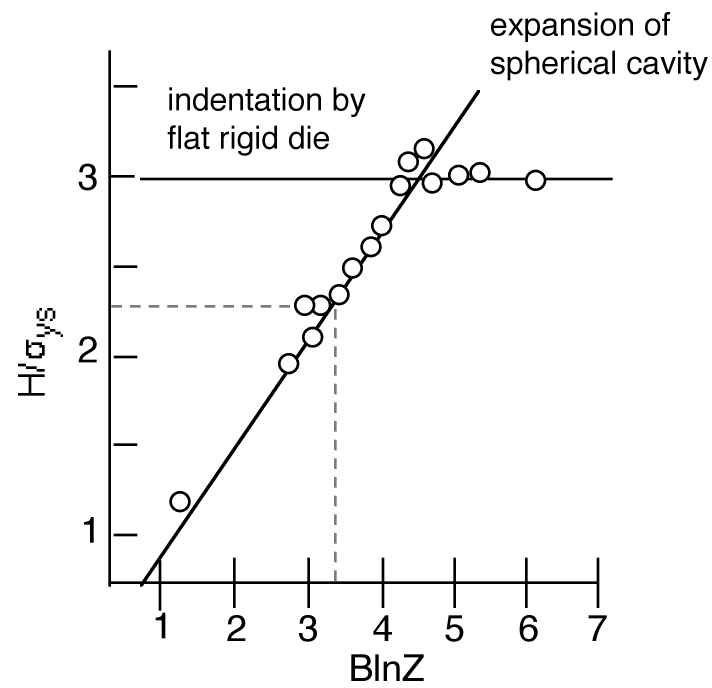


Figure II.2. The relationship derived by Marsh (1963) gives a strength of 115 MPa for the epoxy films of this study.

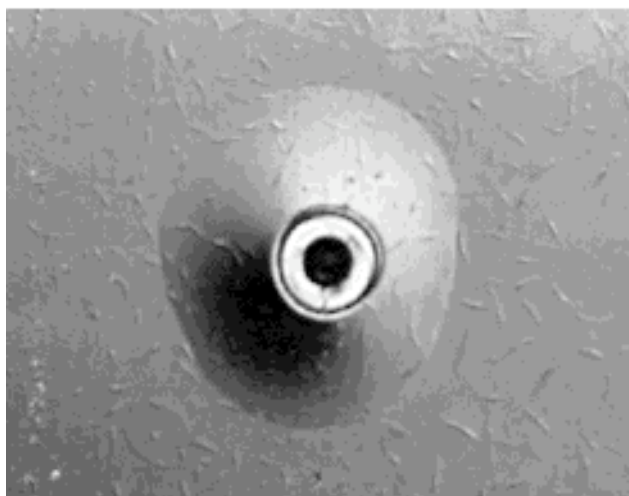


Figure II.3. The 11.8 μm thick epoxy film delaminated during indentation. The extent of delamination is clearly seen in this optical image.

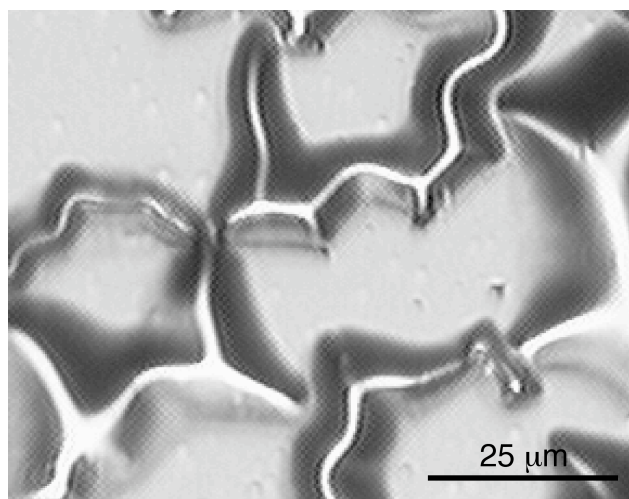


Figure II.4. Stressed overlayers triggered extensive telephone cord blistering in the 24 nm thick epoxy film.

film. Nanoindentation was then used to induce interfacial fracture in the films where spontaneous telephone cord blistering did not occur. Tests on the 164 and 615 nm thick films triggered isolated instances telephone cord blistering and also triggered formation of large circular blisters on the 164 nm thick epoxy film. (Figure II.5a) (Moody et al., 2001) There was no excursion or discontinuity in the load versus displacement curve defining the onset of fracture as often observed in hard metal and ceramic films. (Bagchi et al., 1994; Bagchi and Evans, 1996; Zhuk et al., 1998) (Figure II.5b) Spall size was also independent of maximum load and indenter displacement. Close examination of the indentations and the blisters using atomic force microscopy showed that material was not compressed into the tungsten overlayer. Instead, the overlayer wrapped around the indenter, increasing the effective indentation size. This strongly suggests that indentation served to nucleate fracture, but once fracture nucleated, delamination and blister formation were driven by the residual stresses in the tungsten overlayer. Moreover, since material was not compressed into the overlayer during indentation, there was no increase in the overlayer stress.

II.1.3.5 Interfacial Fracture Surface Analysis

We were unable to determine whether epoxy remained on the substrate surface as previously observed for films on glass (Swadener et al., 1999; Agrawal and Drzal, 1995a,b) or whether failure occurred along the film-substrate interface as observed for this film system on aluminum. (Kent et al., 2000) However, we used a peel test to remove some blistered films from the aluminized substrates and then examined the substrates using optical microscopy with Nemarski contrast and attenuated total reflectance spectroscopy. The AFM results are shown in Figure II.6 In both test procedures, no epoxy was observed on the substrates strongly suggesting that failure occurred interfacially.

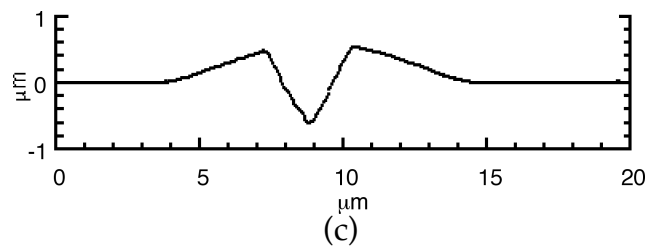
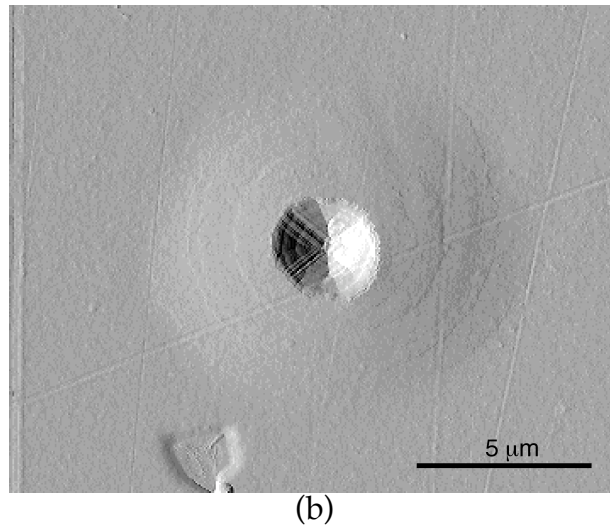
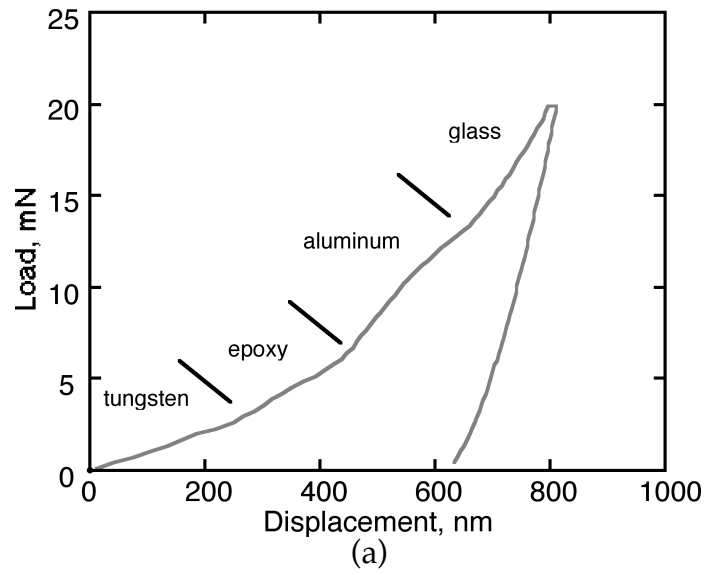
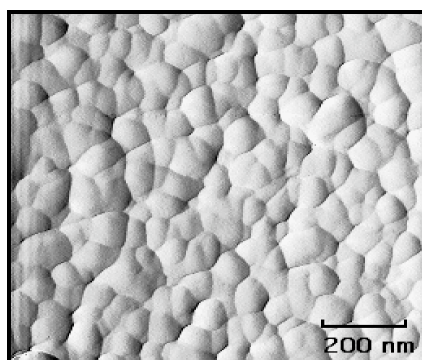
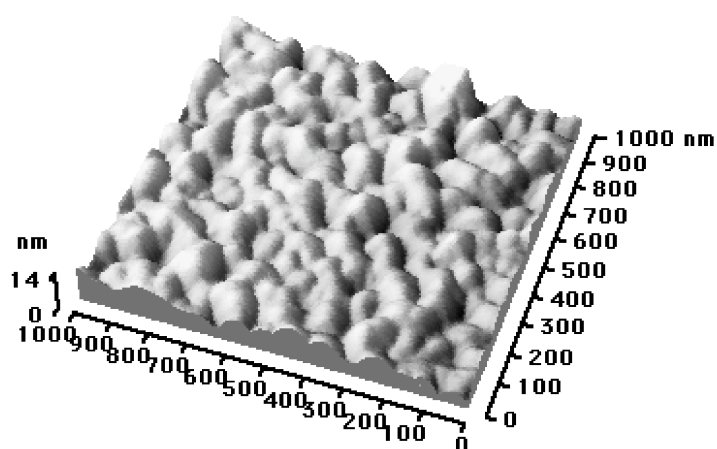


Figure II.5. (a) Indentation tests exhibited no excursion or discontinuity in the load versus displacement curve. The indentations triggered formation of (b) large circular blisters on the 164 nm thick epoxy film. (c) Atomic Force Microscopy of the blister further showed that material was not compressed into the film.



(a)



(b)

Figure II.6 Atomic Force Microscopy of the aluminum substrate surface, (a) top down and (b) 3-D profile views, showed no evidence of epoxy after testing. The average aluminum film grain size was 100 nm with an rms roughness of 7 nm.

II.1.4 Fracture Energy Analysis

II.1.4.1 Asymmetric DCB Fracture

Interfacial fracture toughness was first measured for an 828/T403 epoxy on aluminum Asymmetric Double Cantilevered Beam Sandwich sample giving a measured fracture energy of 19 J/m² with a standard deviation of 3 J/m².

II.1.4.2 Thick Film Indentation Delamination

The delaminations provided the data from which interfacial fracture energies were determined in the 11.8 μ m thick film. Fracture energies were estimated (Strojny et al., 2000) following the analyses of Thouless, (1988), Ritter et al. (1989), and Rosenfeld et al. (1990) for films where in-plane indentation stresses drive interfacial fracture. In this analyses, delamination is assumed to initiate from an internal discontinuity of radius a , the contact radius. The delaminated region is modeled as an elastic disc under plane stress, incorporating only radial and circumferential stresses. The boundary conditions are such that the external circumference at the edge of the discontinuity is constrained at a distance of $r=b$, the interfacial crack radius. The parameters of the crack analysis are shown in Figure II.7. Integrating the normal stress and strains over the delaminated film volume gives the following strain energy release rate for fracture, (Thouless, 1988; Ritter et al., 1989; Rosenfeld et al., 1990)

$$G(\sigma) = \frac{2\sigma^2 \nu_f^2 h}{E_f + \nu_f + (b/a)^2 (1 - \nu_f)} \quad (3)$$

where ν_f and E_f are Poisson's ratio and modulus of the film respectively, h is the film thickness, b is the delamination radius, and σ_0 is the uniform radial stress on the edge of the contact zone. Assuming that hardness, H , is constant through

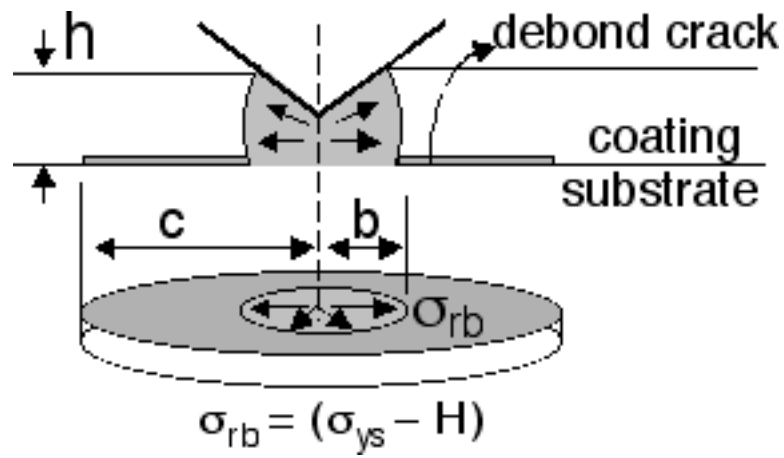


Figure II.7. Delamination in the 11.8 μm thick film is modeled as an elastic disk under plane stress. Only radial and circumferential stresses are used in obtaining fracture energy. (Thouless, 1988; Ritter et al., 1989; Rosenfeld et al., 1990)

the film thickness, σ_o is set equal to $(H - \sigma_{ys})$. With E set to 4.35 GPa, ν equal to 0.38, and a uniform radial stress equal to 141 MPa, equation (3) shows that the fracture energy for 11.8 μm thick Epon 828/T403 film on aluminum averaged $3.6\text{J}/\text{m}^2$. These data are given in Table II.1 and plotted in Figure II.10.

II.1.4.3 Thin Film Telephone Cord Blister Formation

Interfacial fracture energies were obtained for films that exhibited telephone cord blistering using solutions for film systems where residual stresses drive fracture. These solutions were originally derived for single layer film-on-substrate systems (Hutchinson and Suo, 1992; Marshall and Evans, 1984; Evans and Hutchinson, 1984). Work by (Bagchi et al., 1994; Bagchi and Evans, 1996), and more recently by Kriesse et al. (1998,1999) extended these solutions to multilayer systems by treating the multilayer film as a single film of the same total thickness with a transformed moment of inertia. The blister is modeled as a wide, clamped Euler column of width $2b$ for a blister to form between the multilayer film and substrate under these conditions, the compressive residual stress, σ_r , must exceed the stress for interfacial delamination, σ_b , as follows (Kriesse et al., 1999; Hutchinson and Suo, 1992),

$$\sigma_b = \frac{\sigma_o^2}{Bhb^2} \left(\frac{E_{ep}}{\sigma_o^2 \nu_{ep}} \right) (I_T) \quad (4)$$

In this expression, ν_{ep} is Poisson's ratio for the epoxy film, b is the blister half-width, h is the combined tungsten and epoxy film thickness, and B is the unit width, which cancels when multiplied by the transformed moment of inertia. I_T is the transformed moment of inertia for the multilayer film system (Kriesse et al., 1999)

$$I_T = \frac{1}{12} bh_1^3 + A_1 \bar{y}_1^2 + \frac{1}{12} n_a bh_2^3 + A_2 \bar{y}_2^2 \quad (5)$$

where

$$\bar{Y} = \frac{\sum (A_k \bar{y}_k)}{\sum (A_k)} = \frac{\bar{y}_1 A_1 + \bar{y}_2 A_2}{A_1 + A_2} \quad (6)$$

with

$$A_1 = b h_1 \quad (7a)$$

$$A_2 = n_a b h_2 \quad (7b)$$

$$\bar{y}_1 = h_1 / 2 \quad (7c)$$

$$\bar{y}_2 = h_1 + h_2 / 2 \quad (7d)$$

$$n_a = \frac{E_W \sum \epsilon_{ep}^2}{\sum \epsilon_W^2 E_{ep}} \quad (7e)$$

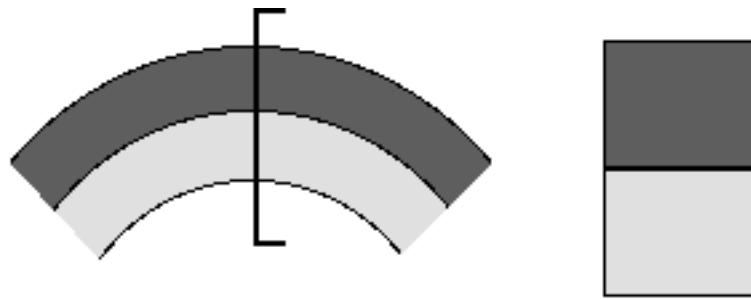
The model parameters are schematically shown in Figure II.8.

The residual stress can then be determined from the blister height and the stress for delamination as follows (Hutchinson and Suo, 1992),

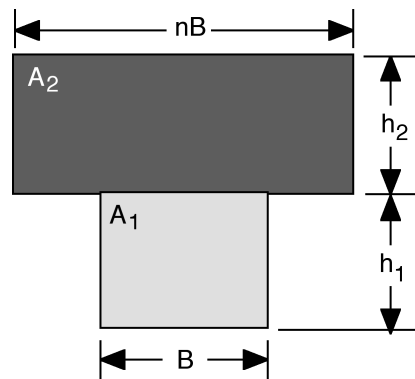
$$\sigma_r = \sigma_b \frac{3\epsilon^2}{4h^2} + 1 \quad (8)$$

where ϵ is the buckle height and σ_b is given by equation (4).

Optical profilometry and AFM were used to measure blister heights and widths. Measurement location and schematic blister profile are shown in Figure II.9. Combining these measurements with the elastic modulus and Poisson's ratio for Epon 828/T403, a compressive residual stress of -2.1 GPa was calculated for the tungsten overlayers on the epoxy films. This value is in good agreement with compressive stress measurements of -2.2 GPa from tungsten on glass samples run under identical deposition conditions in the same sputter chamber. This agreement supports the application of these mechanics-based, elastic isotropic solid models for estimating interfacial fracture energies in this thin epoxy film system.

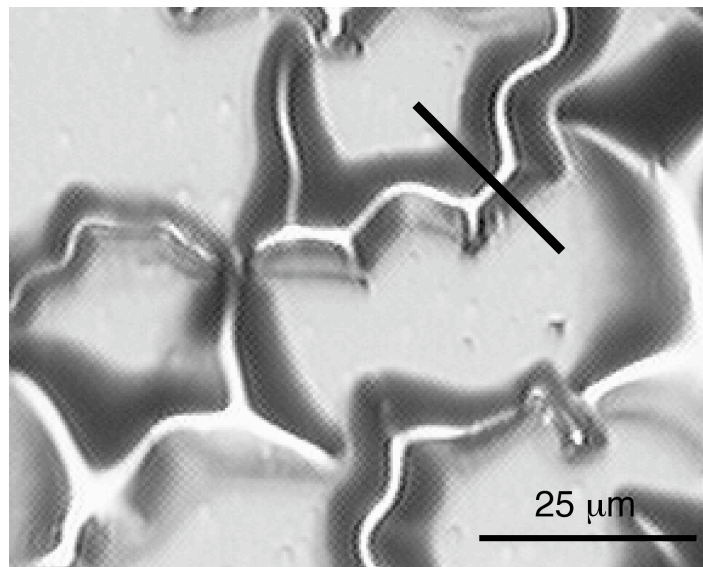


(a)

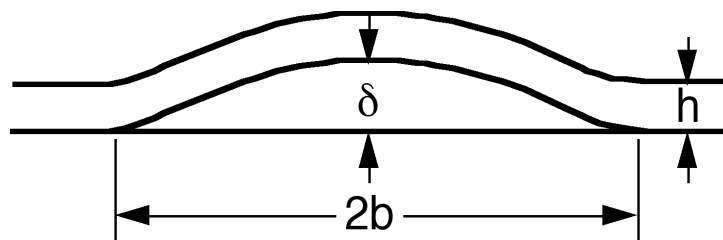


(b)

Figure II.8. Schematic showing model parameters used to determine transformed moment of inertia. (a) Bending and cross-section. (b) Equivalent moments. From Kriese et al., (1999).



(a)



(b)

Figure II.9. (a) Measurement location and (b) schematic of a telephone cord blister profile.

The residual stress and stress for delamination were then used to determine the strain energy release rate for interfacial fracture along the straight side wall portions of the telephone cord blisters from,

$$G(\sigma) = \frac{\sigma^2 h^2}{2E} (\sigma_r + \sigma_b) (\sigma_r + 3\sigma_b) \quad (9)$$

In this expression, E and ν are weighted elastic modulus and Poisson's ratio as follows, (Kriese et al., 1999)

$$E = \frac{E_{ep} h_{ep} + E_w h_w}{h_{ep} + h_w} \quad (10a)$$

$$\nu = \frac{\nu_{ep} h_{ep} + \nu_w h_w}{h_{ep} + h_w} \quad (10b)$$

where h , is the combined tungsten and epoxy film thickness, σ_r , is the bilayer residual stress, and σ_b , is the bilayer delamination stress. The measured fracture energies are given in Table II.2 and Figure II.10. These results show that fracture energies approach a lower limiting value but this value varies with blister morphology.

II.1.4.4 Thin Film Circular Blister Formation

In the regions of the epoxy films that did not blister on deposition of the tungsten overlayer, nanoindentation was used to trigger delamination and blister formation. In most tests, indentation triggered telephone cord blister formation. However in some tests on the 164 nm thick epoxy film, indentation triggered circular blister formation. The center was unconstrained with blister formation occurring on release of the load. An AFM circular blister image and blister profile are shown in Figure II.11. For small buckling deflections, Marshall and

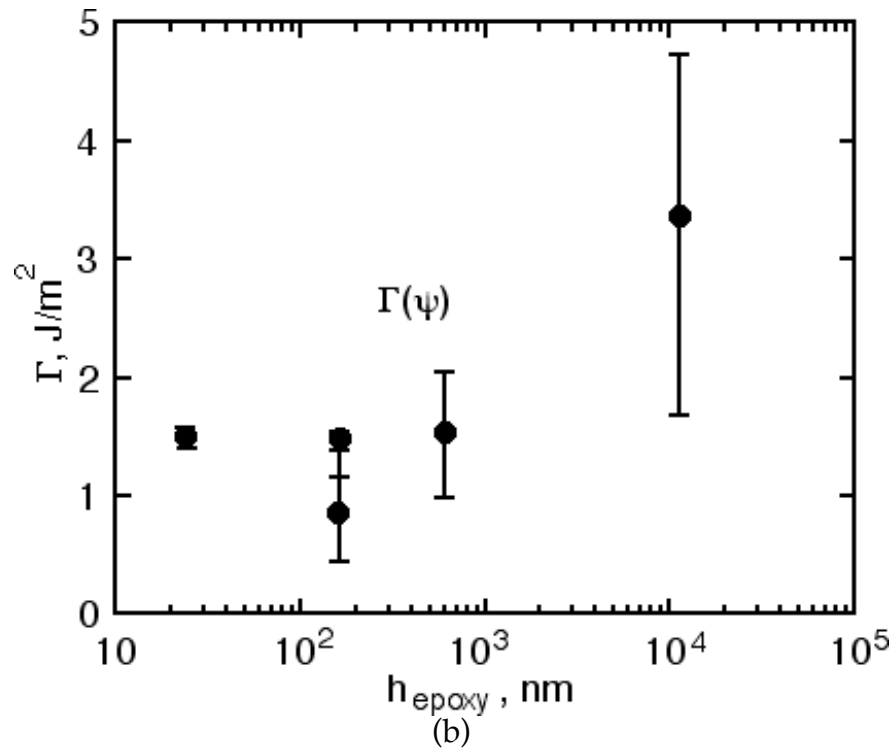
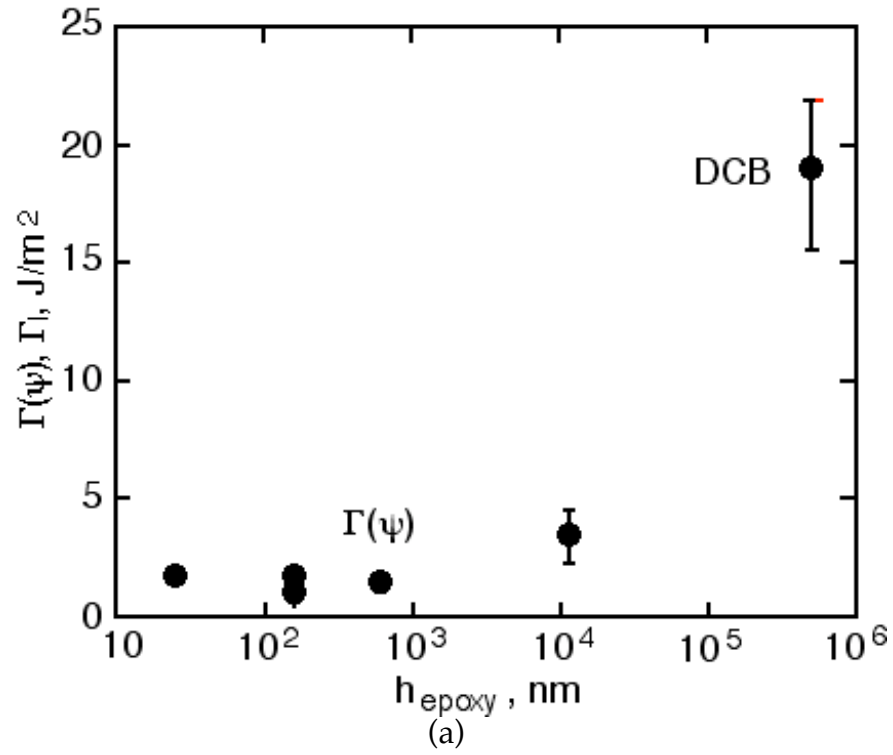
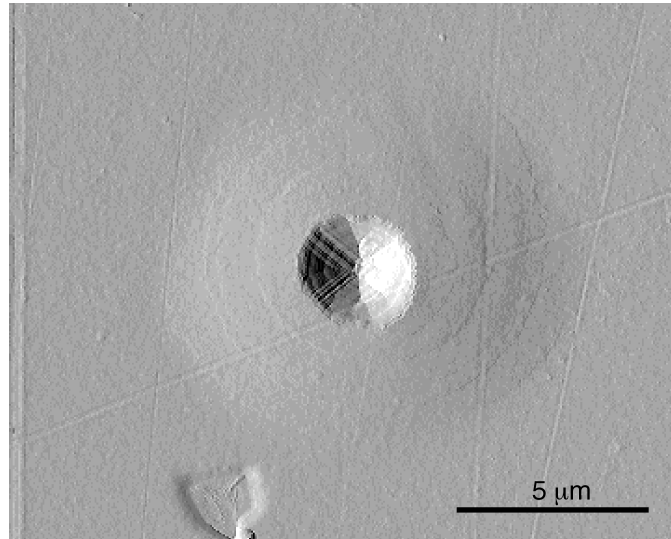
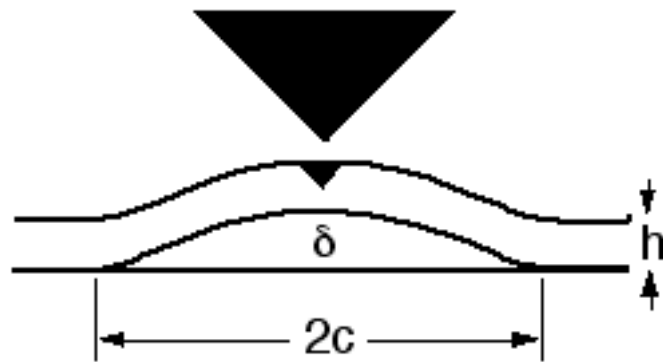


Figure II.10. (a) Fracture energies decreased with decreasing film thickness reaching a lower limiting value near 1.5 J/m². (b) Measured energies varied with blister morphology with the lowest values from circular blister measurements.



(a)



(b)

Figure II.11. (a) An AFM image of a circular blister and (b) a typical circular blister profile.

Evans (1984) and Evans and Hutchinson (1984) derived an asymptotic solution for strain energy release rate by modeling the blister as a clamped circular plate with a radius much greater than the film thickness and subject to an equibiaxial compressive stress. For a blister to form between the multilayer tungsten-epoxy film and the substrate, the compressive residual stress, σ_r , must exceed the stress for interfacial delamination, σ_c given as follows (Kriese et al., 1999)

$$\sigma_c = \frac{k}{Bha^2} \left[\frac{E_{ep}}{(1 - \nu_{ep}^2)} \right] (I_T) \quad (11)$$

where a is the blister radius.

The residual stress can then be determined from the blister height and the stress for delamination as follows, (Hutchinson and Suo, 1992)

$$\sigma_r = \sigma_c \left[C \frac{h^2}{b^2} + 1 \right] \quad (12)$$

where $C = 0.2473(1 + \nu) + 0.2231(1 - \nu^2)$ and b is the buckle height. Combining blister height and radii measurements from atomic force microscopy with thickness-weighted elastic moduli and Poisson's ratios (Kriese et al., 1999), a compressive residual stress of -1.9 GPa was calculated for the tungsten overlayer from measured blister heights. This value is in good agreement with compressive stress measurements of -2.1 GPa from telephone cord blisters and -2.2 GPa from tungsten on glass samples run under identical deposition conditions in the same sputter chamber. This agreement further supports the application of these mechanics-based, elastic isotropic solid models for estimating interfacial fracture energies in this thin epoxy film system.

The residual stress and stress for delamination were then used to determine the interfacial fracture energy using,

$$G(\sigma) = \frac{(1 - \nu) h \sigma^2}{E [1 + 0.9021(1 - \nu)]} \left[\frac{b}{h} \right] \left[\frac{\sigma_r}{\sigma_c} \right] \left[\frac{b}{h} \right] \quad (13)$$

where E and ν are the thickness-weighted elastic modulus and Poisson's ratio for the multilayer film. (Kriesse et al., 1999) Substituting the appropriate values into equation (13) gives a fracture energy of 0.9 J/m^2 . (Table II.3 and Figure II.10) This value is somewhat lower than the corresponding telephone cord blister value due to differences in crack tip loading conditions between telephone cord and circular blisters. (Hutchinson and Suo, 1992)

II.1.4.5 Mode I Fracture Energies

Interfacial fracture is often treated as a mode I failure with mode I energies at crack arrest set equal to the practical work of adhesion (Hutchinson and Suo, 1992). The measured fracture energies are comprised of mode I normal and mode II shear contributions and varies with blister morphology. Several criteria have been proposed to characterize contributions based on the phase angle of loading, ψ . This angle is defined as the tangent of the ratio between shear and normal forces at the crack tip. Of these criteria, the following relationship is often found to realistically reproduce data for interfacial fracture (Hutchinson and Suo, 1992),

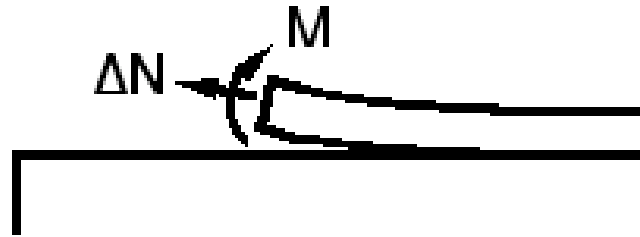
$$\psi_I = \frac{\psi(\psi)}{\left\{1 + \tan^2 \left[(1 - \psi) \psi \right] \right\}} \quad (14)$$

where ψ is a material parameter equal to 0.3 for most materials. It should be noted that significant reservations have been raised concerning determination of the phase angle for multilayer systems (Kriesse et al., 1999) especially when crack growth is accompanied by significant plastic deformation (Wei and Hutchinson, 1998; Tvergaard and Hutchinson, 1993; Volinsky et al., 1999). Relatively low measured fracture energies and thin films suggest that plastic deformation is not a significant factor in interfacial fracture for the films of this study. The phase angle of loading was then estimated using the following equation for telephone cord and circular blister formation as follows (Hutchinson and Suo (1992),

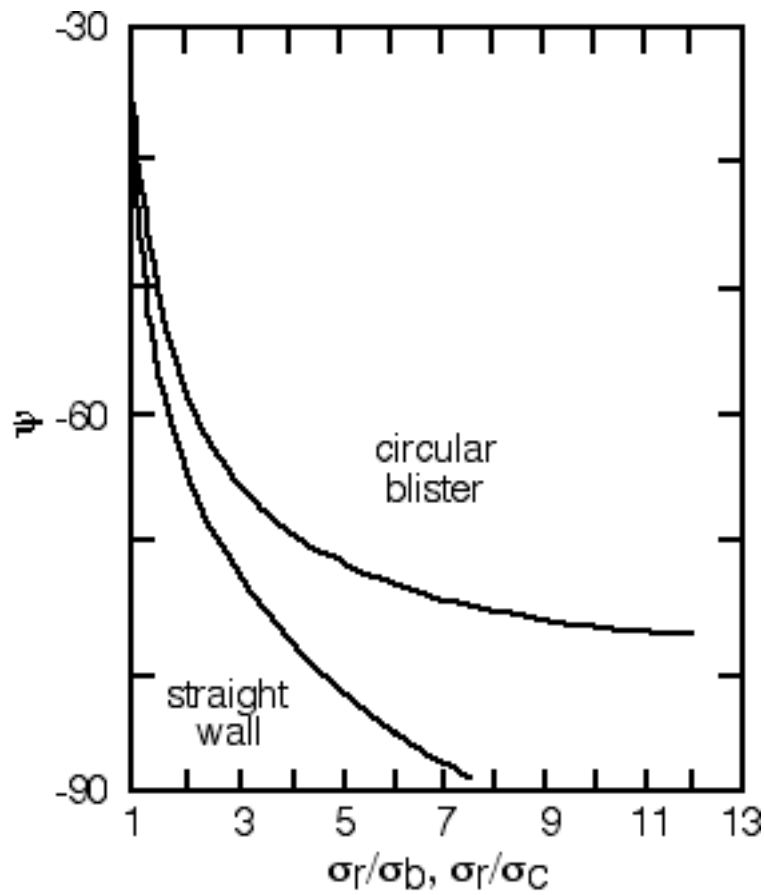
$$\phi = \tan^{-1} \frac{\cos \phi + \frac{h \Delta N}{\sqrt{12} M} \sin \phi}{\sin \phi + \frac{h \Delta N}{\sqrt{12} M} \cos \phi} \quad (15)$$

In this equation, ΔN is the in-plane stress, M is the bending moment, and ϕ is a dimensionless function describing the elastic mismatch between the film and the substrate. The value for $h \Delta N / (\sqrt{12} M)$ is determined from numerical solutions based on an effective driving force of σ_r / σ_b for telephone cord blisters and σ_r / σ_c for circular blisters. (Hutchinson and Suo, 1992) The solutions are shown in Figure II.12. Accounting for the effect of elastic mismatch between the epoxy and aluminum, ϕ is set equal to -53.1° . (Suo and Hutchinson, 1989) With these values, the phase angles of loading for blisters in the 24, 164 and 614 nm thick films were determined using equation (15). The phase angle of loading for the delamination fracture of the 11.8 μm thick films was equal to 37° . (Hutchinson and Suo, 1992; Moody et al., 2002)

Mode I fracture energies were determined for all tests with the results listed in Tables II.1, II.2, and II.3 and plotted in Figure II.13. The results provide a unique set of data with film thickness spanning five orders of magnitude and show that the measured fracture energies decrease with decreasing film thickness to a value of 1.6 J/m^2 for the 24 nm thick film. Of particular note, the mode I telephone cord and circular blister 164 nm thick film fracture energies superimpose providing additional support for use of this elastic based fracture energy approach. (Figure II.13b) The lower limiting mode I value of 0.5 J/m^2 is significantly higher than the true work of adhesion for uncured epoxy oligomers on a methyl-terminated aluminum surface of 50 mJ/m^2 . (Kent et al., 2000) However, it must be noted that this low value does not account for chemical interactions that may form upon cure. The value near 0.5 J/m^2 may indicate that we have irreversible specific interactions such as hydrogen-bonding. If irreversible interactions form upon curing, the 'true work of



(a)



(b)

Figure II.12. (a) Schematic of blister cross-section showing moments and loads from which (b) phase angles of loading for circular and telephone cord (straightwall) blisters were calculated as a function of effective driving force. From Hutchinson and Suo (1992)

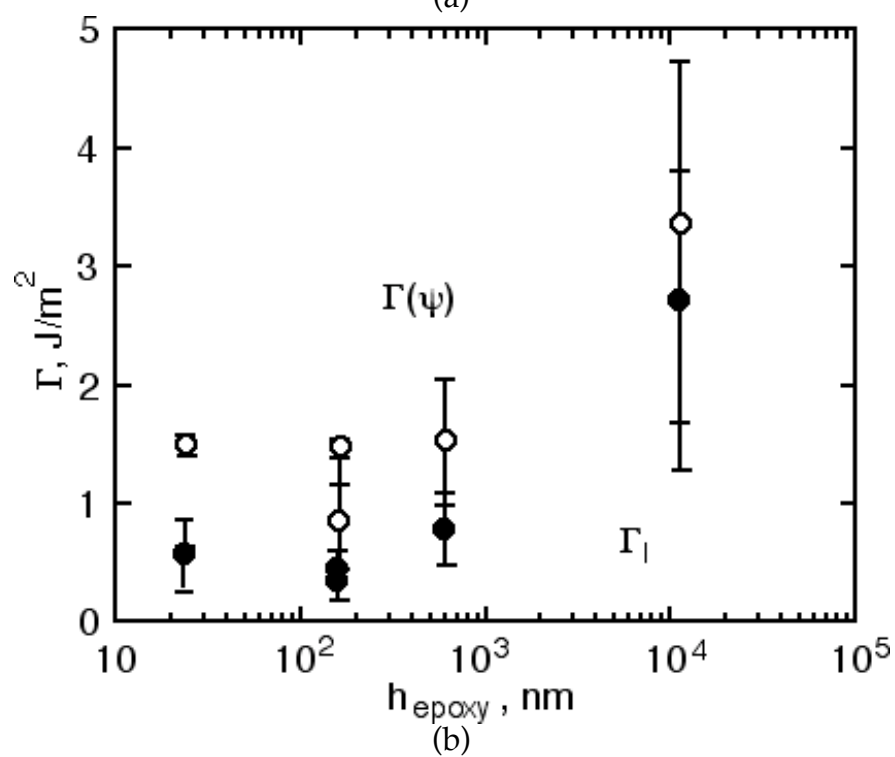
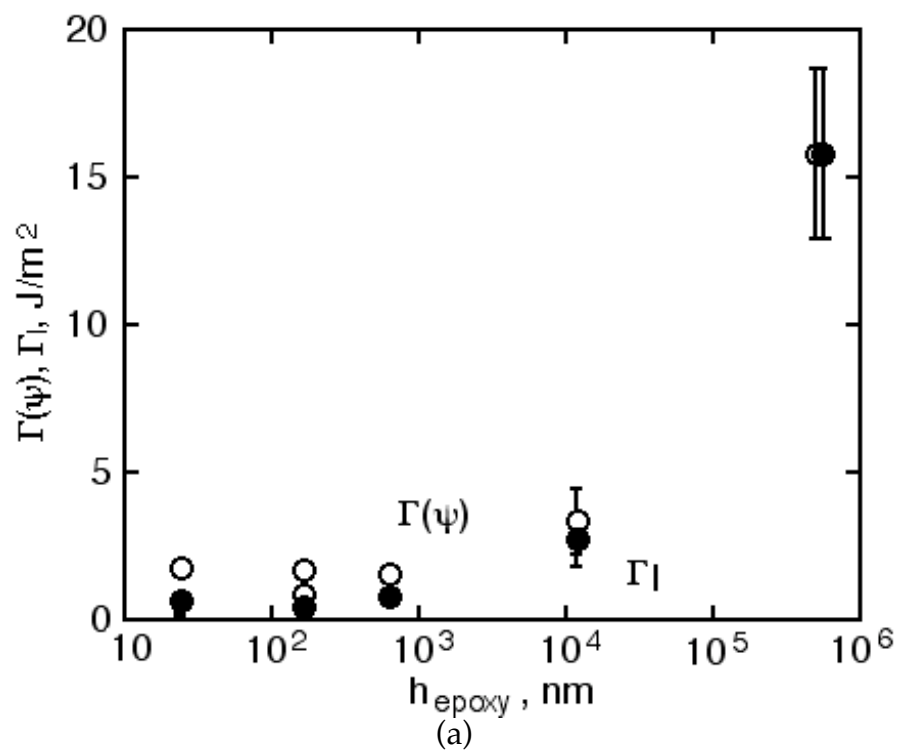


Figure II.13. (a) Mode I fracture energies decrease to a lower limiting value near 0.5 J/m^2 . (b) The mode I components of the measured fracture energies from telephone cord and circular blisters superimpose.

adhesion' is undefined. Then 0.5 J/m² may be near the fundamental value for such an interaction, or the 'practical work of adhesion'.

II.1.4.6 Crack Tip Opening Angle Approach

An approach based on slow crack growth provides a second method for determining mode I contributions and a validation for use of the Hutchinson and Suo (1992) elastic approach to describe the relationship between mode I and mode II contributions. The telephone cord blisters in the epoxy films grew slowly across the samples. Estimation of crack tip plastic zone sizes using a plastic strip model (Volinsky et al., 1999) shows that the plastic zones traverse only partway through the films. The plastic zone sizes are probably much smaller than calculated due to overlayer constraint and fall within the criteria for small scale yielding in thin films discussed by Wei and Hutchinson (1998). Assuming that interfacial fracture in thin films at low fracture energies occurs under small scale yielding conditions, Volinsky and Gerberich (1999) have modeled the threshold for crack growth susceptibility in thin films using the tearing modulus approach derived by Rice, Drugan, and Sham (RDS), (1980)

$$T_o = \frac{E\Delta_c}{\sigma_{ys}r_m} \left[\frac{\sigma}{\sigma_{ys}} \ln \left(\frac{e\sigma EJ_o}{r_m \sigma_{ys}^2} \right) + \frac{E\Delta_c}{\sigma_{ys}r_m} \right] \quad (16)$$

In this expression, T_o is the tearing modulus, Δ_c is the crack displacement at a distance r_m behind the crack tip, $\sigma \approx 1$, $\sigma \approx 2$, e is the natural logarithm base, E and σ_{ys} are the elastic modulus and yield strength of the film respectively, σ is a constant equal to 5.1, and J_o is the threshold value of the J integral at crack initiation. For films with relatively low interfacial fracture toughness, as for the films in this study, the first term dominates leading to the simplified approximation.

The tearing modulus can then be used to describe the relationship between steady state, J_{ss} , and threshold strain energy release rates for crack growth as follows (Rice et al., 1980),

$$J_{ss} = J_o \exp \left(\frac{\sigma_c T_o}{r_m} \right) \quad (17)$$

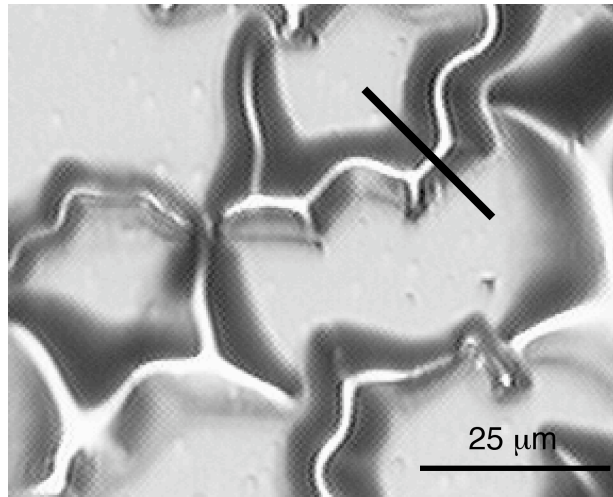
Substituting equation (16) for T_o , expressing σ_c/r_m as the crack tip opening angle (CTOA), and rearranging terms gives the following expression for threshold strain energy release rate,

$$J_o = J_{ss} \exp \left(\frac{\sigma_{ys}}{E \cdot \text{CTOA}} \right) \quad (18)$$

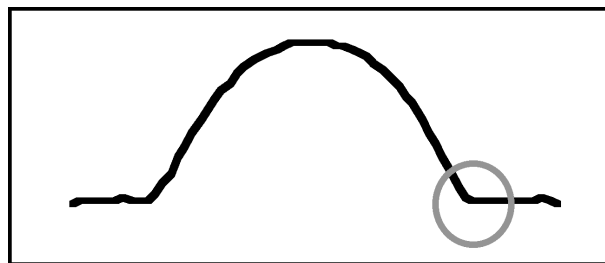
Yield strengths of free surface thin polymer films are often determined from measured hardness values using the relationship derived by Marsh (1963). CTOA values were determined from measured profiles from telephone cord blisters in the 615 nm thick film and circular blisters in the 164 nm thick film as illustrated in Figure II.14. J_o values were then calculated for the 164 and 615 nm thick epoxy films from equation (18) using the measured elastic modulus for Epon 828/T403 and appropriate yield strength and CTOA values. Measured fracture energies were substituted for J_{ss} . The results in Table II.4 show there is agreement between results from the mechanics based and the ductile crack growth CTOA models. The agreement also supports the use of equations (14) and (15) to describe the relationship between mixed mode and mode I fracture energies and the confidence that the measured values accurately describe resistance to interfacial fracture for these film systems.

II.1.5 Summary

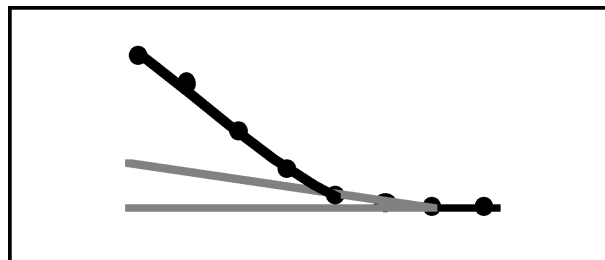
In this study we combined nanoindentation with stressed overlayers to determine the effect of film thickness on the interfacial fracture energy of Epon 828/T403. The films were spin coated onto aluminized substrates to four thicknesses ranging from 24 nm to 11.8 μ m. Nanoindentation gave a near surface



(a)



(b)



(c)

Figure II.14. (a) Measurement location, (b) profile, and (c) crack tip opening angle (CTOA) across a telephone cord blister.

elastic modulus of 4.35 GPa and a hardness equal to 250 MPa with a film strength of 115 MPa. The combination of nanoindentation and deposition of a highly stressed tungsten overlayer were used to induce delamination and blister formation in the films. Interfacial fracture energies were then determined using mechanics-based models modified for multilayer films. Interestingly, the results parallel thin metal film behavior where interfacial fracture energies decreased to 1.6 J/m^2 and mode I components to 0.5 J/m^2 as film thickness decreased to 24 nm. This value is significantly higher than the work of adhesion for uncured epoxy oligomers on a methyl-terminated aluminum surface. Nevertheless, it may indicate that we have irreversible specific interactions such as hydrogen bonding. Then 0.5 J/m^2 may be near the fundamental value for such an interaction, or the 'practical work of adhesion'.

II.2 Self Assembled Monolayers

II.2.1 Background

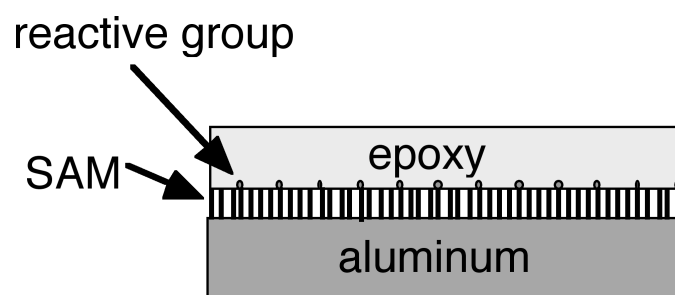
The resistance to failure of an interface is comprised of the work required to rupture bonds (practical work of adhesion) and the work dissipated by inelastic deformation within adjoining materials. High adhesive bond strengths lead to high rates of inelastic deformation. Two recent studies (Kent et al. 2000; Zhuk et al., 1998) have used self-assembled monolayers to study the effects of bond strength on interfacial fracture. Following these studies, we examined the effects of methyl and bromine terminated self-assembled monolayers on adhesion of 828/T403 to aluminum. The methyl groups interact weakly while bromine-terminated groups react strongly with amine-cured epoxies permitting adhesion to be controlled by varying self-assembled monolayer composition. Tests were then run on epoxy bonded samples as a function of SAM composition and bond thickness to define how adhesion controls susceptibility to interfacial failure.

II.2.2 Materials and Procedure

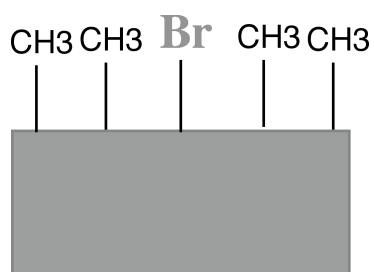
II.2.2.1 SAM systems

The interfacial interactions between epoxy films and aluminum substrates were controlled using mixed self-assembling monolayers of dodecyltrichlorosilane and bromoundecyltrichlorosilane. These monolayers were applied to the polished aluminum surfaces at high density such that the terminal groups determined the interfacial interactions with the epoxy adhesive. (Figure II.15) The methyl groups interact with epoxy through weak van der Waals forces, while the Br-terminal groups interact with epoxy by forming an alkyl ammonium bromide compound with the amine crosslinker. This results in a covalent linkage across the interface through $R-NH_2^+Br^-R'$ bonds. XPS showed there is a direct 1:1 relationship between Br in solution and Br fraction on the aluminum surface. (Figure II.16) A detailed study of the monolayer structure and composition was performed for depositions onto silicon substrates using X-ray reflectivity, TOF-SIMS, AFM, and contact angle measurements. The quality of the monolayer on the aluminum substrates was monitored by contact angle measurements. Depositions onto aluminum substrates were performed in a nitrogen-purged glove box.

Both DCB and Tensile Brazil Nut samples were fabricated with a small section, typically 1/2 in., of bond length coated with purely methyl terminated molecules. This purpose of this was to serve as an extremely sharp starter crack. This was accomplished by first coating the entire surface with a methyl-terminated monolayer, then removing the monolayer from all but the desired end section with UV-ozone (masking the end section with aluminum foil), and finally depositing the mixed monolayer into the area that had been exposed to the UV-ozone. This procedure resulted in a very well-defined and reproducible starter crack region.



(a)



(b)

Figure II.15 Schematic showing (a) a mixed SAM along a substrate interface with (b) methyl and bromine terminated reactive groups.

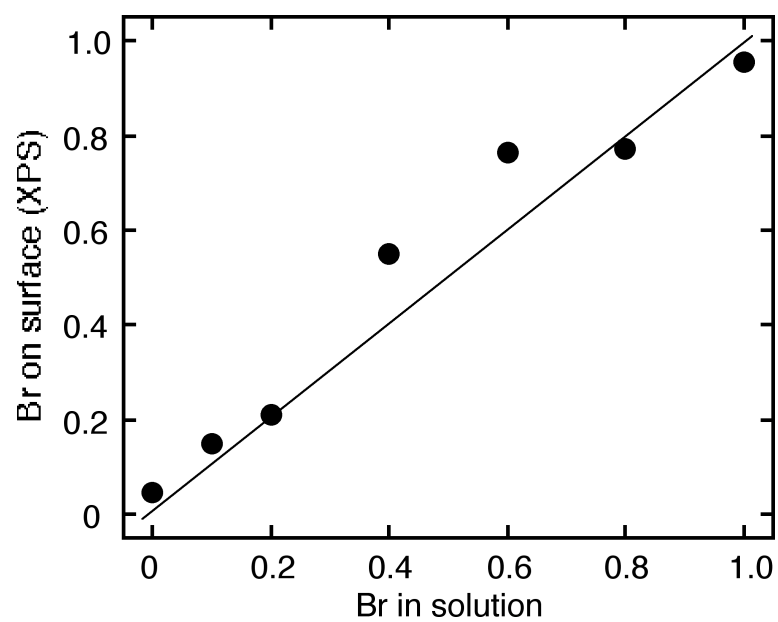


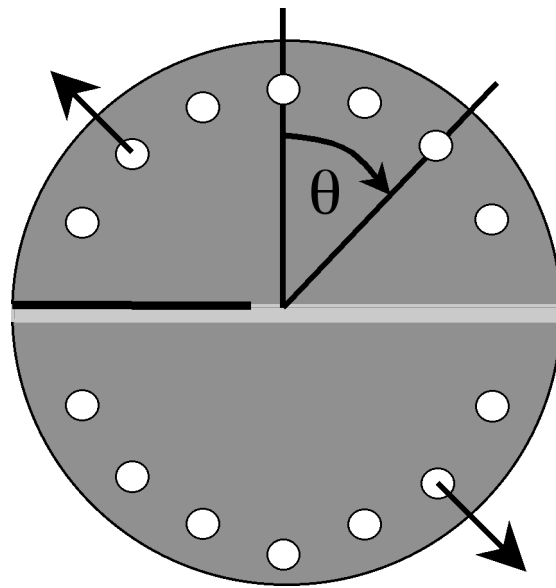
Figure II.16 A one-to-one relationship exist between bromine in solution and bromine on the substrate surface.

II.2.2.2 Tensile Brazil Nut Samples

In addition to the ADCBS specimen described in the previous section, the Tensile Brazil Nut Sandwich (TBNS) specimen was used to measure the interfacial fracture energy of a mm-scale epoxy bond over a wider range of applied mode mixity than could be generated with an ADCBS specimen. This test geometry is similar to one recently used by (Kuhl and Qu, 2000). The specimen consists of two semicircular aluminum disks bonded together by a 0.5-mm thick epoxy layer (Figure II.17). Each 50.8-mm diameter bonded disk is 10.2-mm thick. The specimen is loaded via pins inserted through one of the sets of the opposing 3.2-mm diameter holes that are positioned along a 20.3-mm radius circle. The applied mode mixity can be changed by using different pairs of loading-holes, and a 90 degree variation in applied crack-tip mode mixity is possible. The ability to easily adjust the applied mode mixity over a wide range of potential values is a substantial advantage over other common types of interfacial fracture specimens.

Each TBNS specimen is fabricated separately. Small spacers are bonded to the ends of one of the semi-circular aluminum disks to define the epoxy layer thickness, and the other adherend is subsequently positioned on top. Teflon tape is then applied to the edges of the specimen to contain the epoxy resin. The TBNS specimen is placed in an open cavity RTV fixture to aid handling, and then a syringe with a small diameter tip is inserted through the tape to fill the bond cavity with epoxy. Finally the RTV fixture that contains the specimen is placed in an oven to cure the epoxy.

Unlike the ADCBS fracture specimen, crack growth is unstable in the TBNS specimen. Also crack length is not independently measured during the test and is assumed known. In addition, meaningful and consistent data requires an initially sharp crack, and methods that insert a relatively blunt crack (e.g. use of Teflon tape to define the initial crack) are suspect. For all these reasons, the method used to insert a sharp pre-crack of known length is a crucial to the success of this specimen. In the method used here, a 23-mm long ODTs SAM is



(a)

Figure II.17 (a) A schematic depiction of the Tensile Brazil Nut Sandwich adhesively bonded sample used in this study.

applied to the bonding surface of one of the semicircular disks, and an 18-mm long Teflon tape is applied on top of the SAM. The 5-mm long portion of the SAM that extends beyond the tape insures that an initially sharp arrested crack can be generated. Instrumented tests showed that the crack arrests at the end of the SAM during the pre-cracking step.

The specimen is loaded at a crosshead displacement rate of 0.02 mm/s by means of a load train that utilizes a chain linkage that connects to a pair of loading-holes. Tests were conducted with $\varphi_{r=10^\circ}$ of 2°, -12°, -26°, and -42° by loading diametrically opposing loading-holes with the upper loading-hole located at 0°, -20°, -40°, and -60°, respectively (Figure II.17). A $\varphi_{r=10^\circ}$ of 2° was also generated by loading the two loading-holes closest to the crack plane (i.e., +/-30° from the crack plane). This loading configuration is particularly useful when pre-cracking a specimen since the strain energy release rate level is seven times higher than that generated when the specimen is subject to the same load, but loaded using diametrically opposed 0° loading-holes. Failure load is the only measured quantity in a TBNS fracture test. A calibration function, which depends on failure load, initial crack length, and the position of the loading points, is used to determine interfacial toughness and the associated crack-tip mode mixity.

II.2.3 Fracture Energy Analysis

II.2.3.1 Surface Interactions

The fracture energy of an epoxy/SAM-coated aluminum interface was measured using the ADCBS specimen ($\varphi_{r=0.01\text{ mm}}$ of -8°) with a 1-mm thick epoxy bond. The SAM coating was applied to the polished aluminum surface of the thinner ADCBS adherend; the surface on which interfacial cracking occurs. The interfacial interactions between the SAM and epoxy were systematically varied by using a SAM coating composed of a mixture of methyl and bromine terminated chains. Bromine interacts strongly with epoxy while methyl groups

interact weakly. A continuous variation in surface interactions was obtained by varying the percent of bromine in the mixed monolayer. Figure II.18 plots the measured interfacial fracture energy as a function of the percent of bromine-terminated chains in the coating. The average fracture energy and associated 95% confidence interval are plotted for each specimen tested. The measurements were made using three sets of specimens that were fabricated at different times. To assess reproducibility between sets, each set contained at least two specimens with a 50% bromine-terminated SAM coating. Figure II.18 shows that while there is significant spread in the 50% bromine fracture toughness, the data falls within a relatively compact band. The data clearly indicate that fracture energy is a strong function of the bromine concentration in the mixed SAM coating, and there appears to be a roughly linear variation in interfacial toughness with the percent of bromine-terminated chains. Fracture energy increases by about a factor of twenty as the strength of the interfacial interactions is increased.

The precise relationship between the molecular work of separation and the percent of bromine-terminated chains is not known. At the lower limit of 0% bromine-terminated chains, which corresponds to a SAM surface coating with 100 percent methyl-terminated chains, the molecular work of separation has a value near 0.05 J/m^2 (Kent, Yim, et al. 2001). The interactions in this case are weak (van der Waals forces), and the molecular work of separation equals the reversible work of adhesion. The value of molecular work of separation corresponding to the upper limit of 100 percent bromine-terminated chains is also not known with certainty. It seems likely, however, that the upper limit for the molecular work of separation is on the order of 1 J/m^2 . This value is consistent with the data for the same epoxy but on an aluminum oxide surface (Figure II.10). Epoxy bonds well to aluminum oxide, and the measured interfacial toughness of epoxy films with a thickness of less than $0.1 \text{ }\mu\text{m}$, a thickness at which the molecular work of separation should dominate any bulk dissipation within the epoxy, is about 1 J/m^2 . The ratio of measured fracture toughness to molecular work of separation for a SAM with 0% bromine-terminated chains is quite high, with a value of about forty. Interestingly, the ratio for a SAM with 100 percent bromine-terminated chains also appears to have a value of roughly forty.

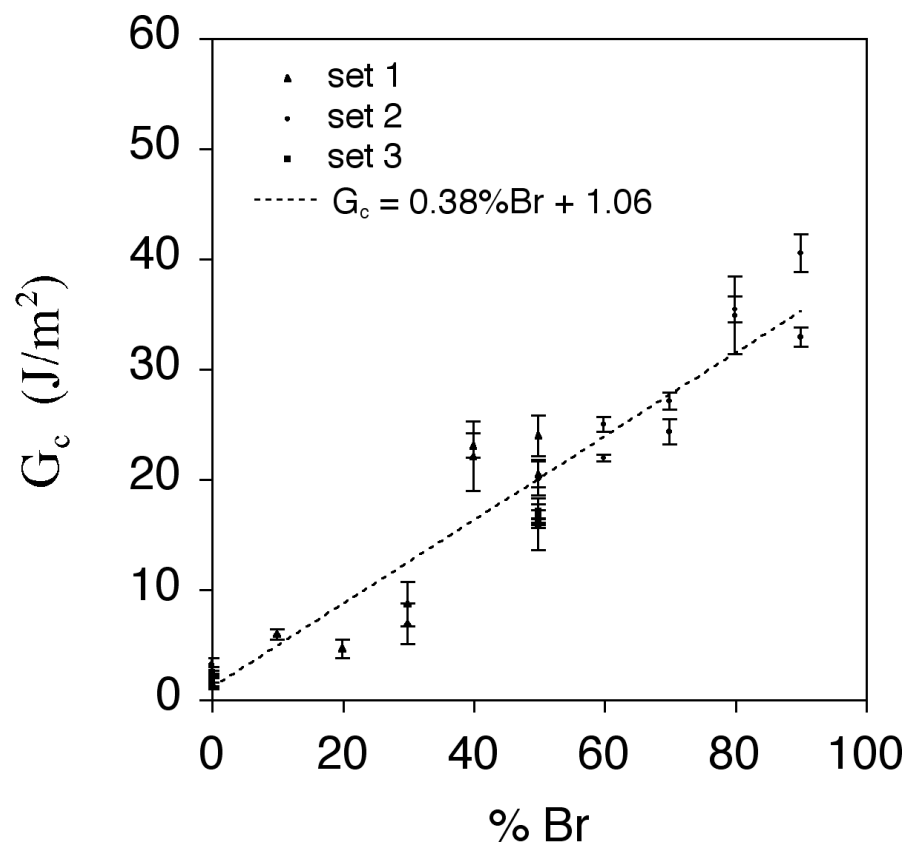


Figure II.18. Variation of G_c with the % of bromine in the mixed monolayer SAM coating (interfacial interactions increase with the % bromine).

II.2.3.2 Bond Thickness

ADCBS specimens with 0.25-mm, 0.50-mm, and 1.0-mm thick adhesive bonds were tested to determine the dependence of interfacial fracture energy on bond thickness when bond thickness is greater than 0.25 mm. A bond thickness independent fracture energy would imply that the small-scale-yielding idealization is applicable. Figure II.19 plots fracture energy vs. bond thickness for an epoxy/SAM-coated aluminum interface with a 50% bromine-terminated SAM, while Figure II.20 plots similar results for a 0% bromine-terminated SAM. The mean G_c value and the associated 95% confidence interval on the mean are plotted for each specimen tested. Specimens with the 50% bromine-terminated SAM coating have quite consistent fracture energy values regardless of bond thickness, with an average value of 16.5 J/m² and a coefficient of variation (standard deviation of the mean values/mean value x 100 %) of 4%. The measured fracture energies for specimens with the 0% bromine-terminated SAM coating are essentially identical for specimens with 0.25-mm and 0.50-mm thick bonds, while results for the 1.0-mm thick bond are somewhat lower than that for the thinner bonds. Note, however, that it is rather difficult to measure fracture energies for very low toughness interfaces like the those of the ADCBS specimens used here where the absolute differences in toughness values for the three bond thicknesses are relatively small. The average fracture energy for specimens with the 0% bromine-terminated SAM is 1.9 J/m² with a coefficient of variation of 23%.

II.2.3.3 Mode Mixity

The variation of fracture energy with mode mixity was measured for an epoxy/SAM-coated aluminum interface with relatively strong surface interactions. TBNS specimens with a 0.5-mm thick epoxy bond and a 75% bromine-terminated SAM-coated aluminum/epoxy interface were tested. Figure II.21 plots fracture energy data for an applied mode mixity ranging from $\square_{r=10^\circ m} = 2^\circ$ to $\square_{r=10^\circ m} = -42^\circ$. The overall trend of the fracture energy vs. $\square_{r=10^\circ m}$ data is

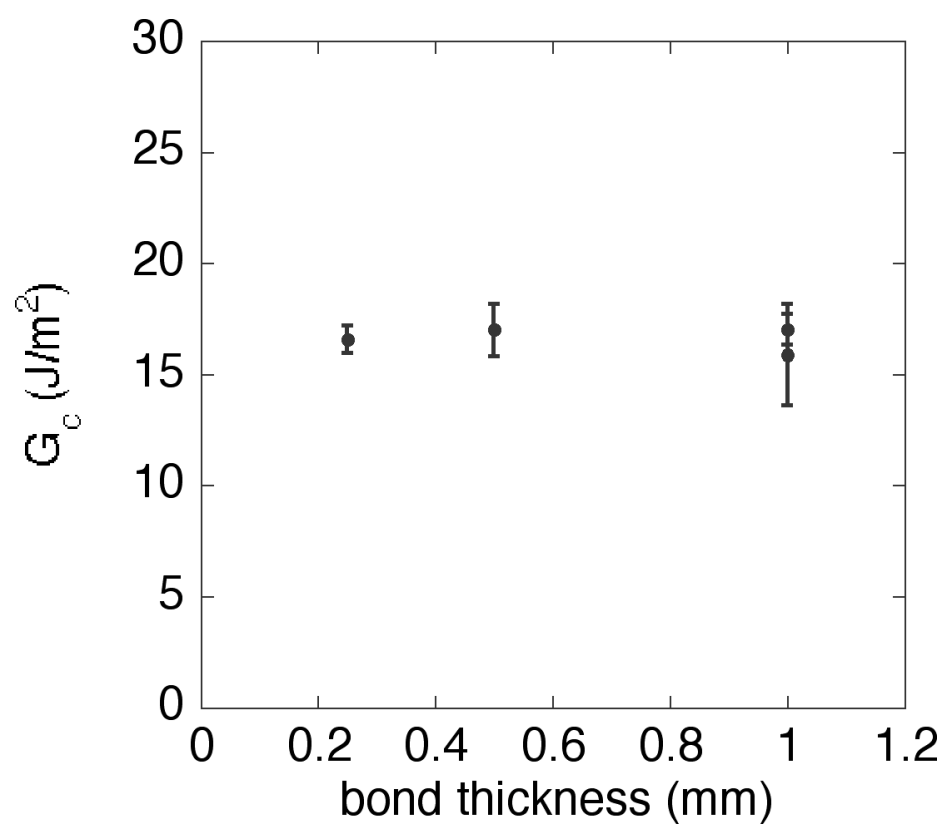


Figure II.19. Variation of G_c with bond thickness for a 50% bromine-terminated SAM coating.

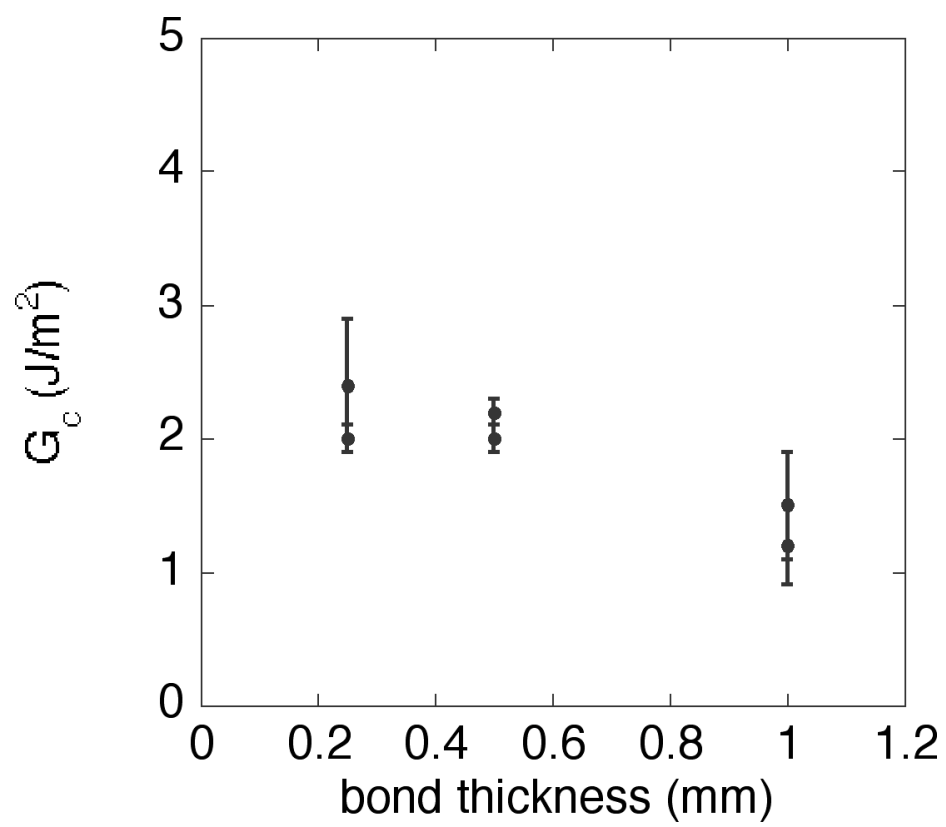


Figure II.20 Variation of G_c with bond thickness for a 0% bromine-terminated SAM coating.

consistent with that observed by others; fracture energy increases substantially with increasing $|\varphi_{r=10^\circ}|$ (Liechti and Chai, 1992; Liang and Liechti, 1995). Eight tests were run with a $\varphi_{r=10^\circ}=2^\circ$ loading. Six of these samples were loaded using the two loading-holes closest to the crack plane (i.e., $\pm 30^\circ$ from the crack plane, referred to as a symmetric loading) while the other two were loaded using the diametrically opposed 0° loading holes (Figure II.17, referred to as the diametral loading). Although the load required to generate the same strain energy release rate values is 2.6 times greater for the diametral loading, the measured fracture energy values are similar. Also note that the measurements were made using two sets of specimens that were fabricated at different times, lending support to the reproducibility of the fabrication process. The average fracture energy value for $\varphi_{r=10^\circ}=2^\circ$ is 37 J/m^2 , with a coefficient of variation of 14% (the 95% confidence interval about the mean is $37 \pm 4 \text{ J/m}^2$). Although ADCBS data was not measured for a 75% bromine-terminated SAM-coated aluminum/epoxy interface, it was measured for essentially similar 70% and 80% bromine-terminated SAM coatings. Those ADCBS results are also plotted in Figure II.21. The TBNS and ADCBS data are in good agreement and consequently confirm the toughness measurements.

II.2.4 Summary

The fracture toughness of aluminum/epoxy interfaces with a range of well-defined interfacial interactions has been measured with an asymmetrical double cantilever beam specimen. Interfacial interactions were varied using self-assembled monolayers containing mixtures of molecules with different terminal groups. The measured interfacial toughness increased by more than a factor of ten as the strength of interfacial interactions was increased. The increase in fracture energy can be attributed to the need for higher stresses and more extensive deformation prior to bond failure.

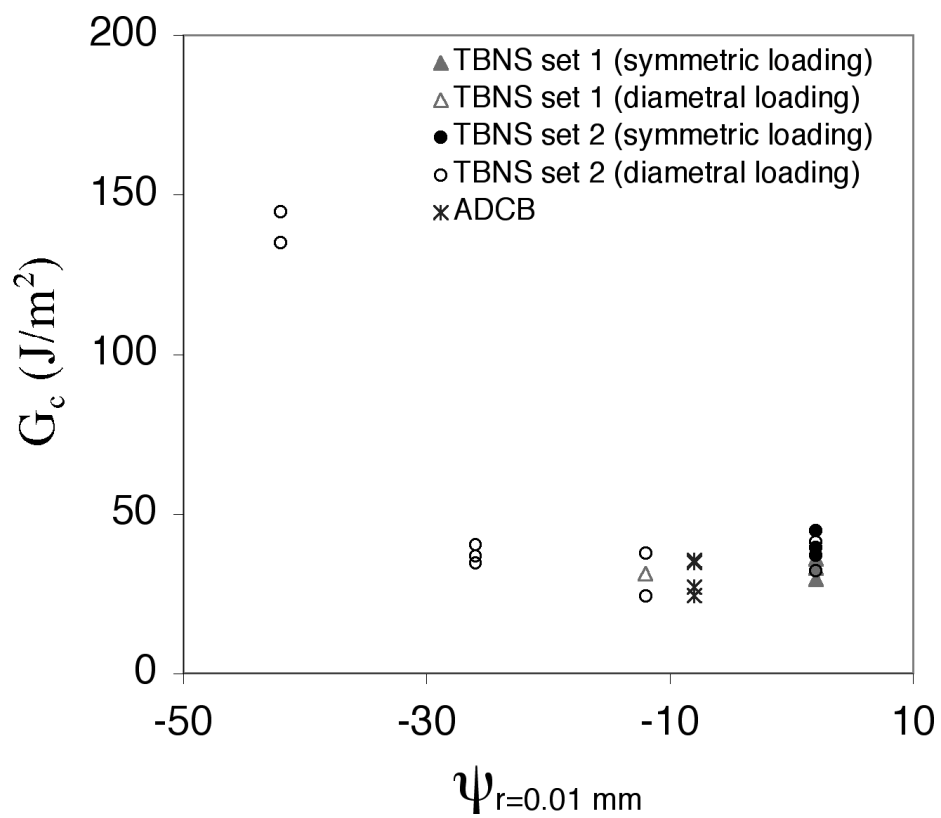


Figure II.21. Variation of the G_c of an epoxy/SAM-coated aluminum interface vs. applied mode mixity (75% bromine mixed monolayer SAM coating).

III. Investigation of Crack Tip Structure Using X-rays

III.1 Background

The use of X-ray scattering and imaging techniques for investigating structural evolution near crack tips was pursued using a pinhole camera operating with a rotating anode source at the UNM, a standard X-ray diffractometer at SNL, and also using the Advanced Photon synchrotron source (Argonne, National Labs). The goal of this work was to determine if this methodology could provide important insights into local crack initiation processes.

III.2 Materials

To initiate this program, we examined a series of polyethylene (PE) and epoxy (EPON 828/T403 and 828/DEA) samples. PE was chosen because it is semicrystalline, and thus produces easily observable diffraction peaks. This allows the best opportunity to develop and assess the methodology. Epoxy is the structural adhesive most commonly used in weapons applications.

III.3 Results

III.3.1 Polyethylene Studies

Initially, bulk samples of PE were examined as a function of draw ratio using a standard diffractometer at SNL with the help of Ralph Tissot and a pinhole SAXS camera at the UNM with the help of Thomas Rieker. The purpose of this background work on bulk samples was to develop a database that would allow us to map the stress or strain fields near crack tips in PE under load. This can be accomplished by finding the boundary regions where the diffraction pattern (crystalline structure) changes. Thin and thick samples approach the limits of plane strain and plane stress, respectively.

III.3.1.1 Background Work on Bulk Drawn Samples

Diffraction data obtained on bulk PE samples for several draw ratios are shown in Figure III.1. Upon drawing, the diffraction pattern changed dramatically as has been documented previously (Butler et al., 1995). This change is due to a stress-induced martensitic transformation in which the orthorhombic structure of undeformed PE is converted to a monoclinic structure. Upon further drawing, the pattern of peaks remained the same but the sharpness (FWHM) changed. In the small angle scattering study, two major changes were observed in the scattering curve with increasing strain as shown in Figure III.2. First, the loss of the peak at $q = 0.03 \text{ \AA}^{-1}$ corresponding to the long period was observed between 0 and 0.2 engineering strain. The long peak corresponds to lamellae-lamellae correlations. Thus, the correlated stacking of lamellae was disrupted at this low strain value. Second, a shoulder appeared at $q = 0.05 \text{ \AA}^{-1}$ which indicates that the crystalline lamellae were oriented with their thin direction ~ -40 to $+40$ degrees from the strain direction.

III.3.1.2 Higher Resolution Studies on Notched Samples

Initial measurements on a notched sample of PE were performed at the APS. The 1 mm thick PE sample was loaded in 3-pt bend until a sharp crack formed. The sample is shown in Figure III.3. X-ray diffraction was obtained near the sharp crack tip with a $300 \text{ \mu m} \times 300 \text{ \mu m}$ beam without load. Data are shown in Figure III.4. No variation in the diffraction pattern was observed around the tip of the crack versus far away from the crack. However, the q range of the data did not extend to sufficiently high values to cover the range where the dramatic changes are expected. So no conclusions can be made at this point. Higher resolution measurements, covering a higher q range, and possibly under load will be carried out during the next available beamtime allocation, scheduled for spring 2003.

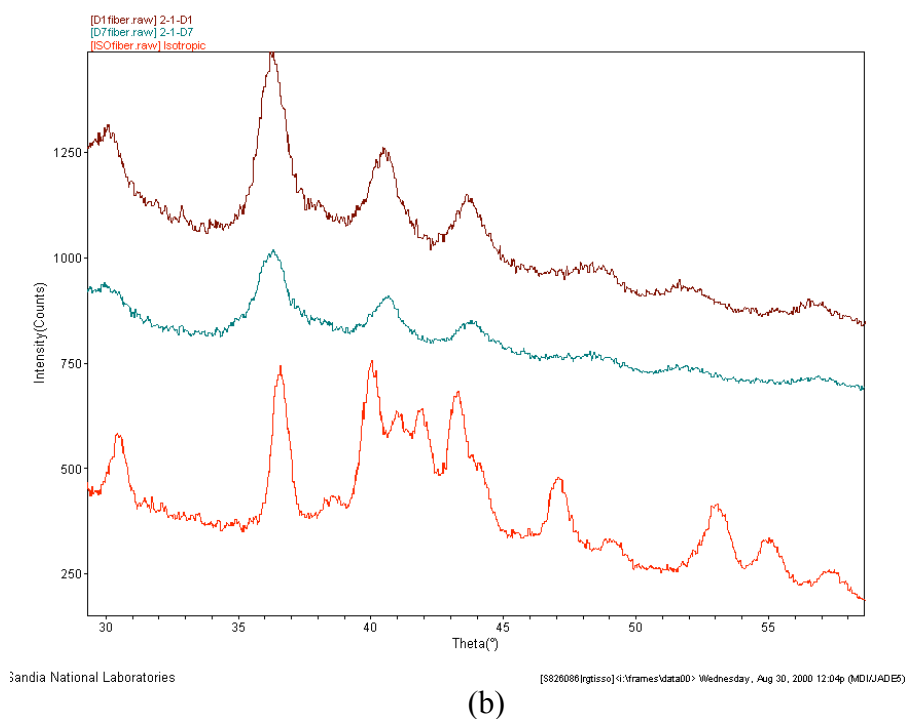
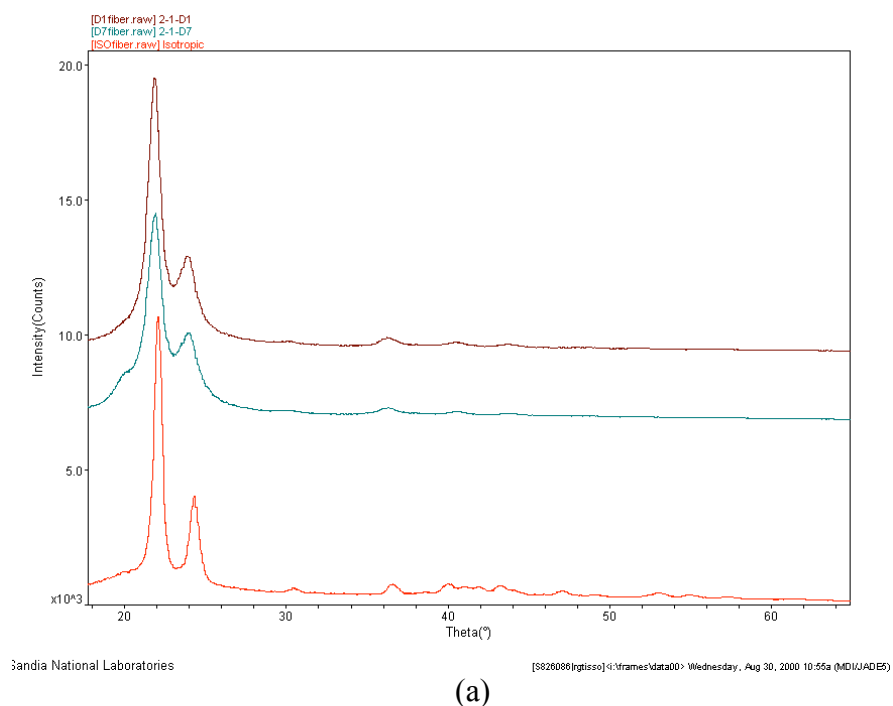


Figure III.1. X-ray diffraction data obtained for a bulk PE sample taken with a standard diffractometer at SNL . Draw ratios are: top curve - 9.45, middle curve – 1.0, and bottom curve – 0.0. The bottom figure is a blow-up of the higher q region where the martensitic transformation is evident. Incident radiation is 1.54 Å.

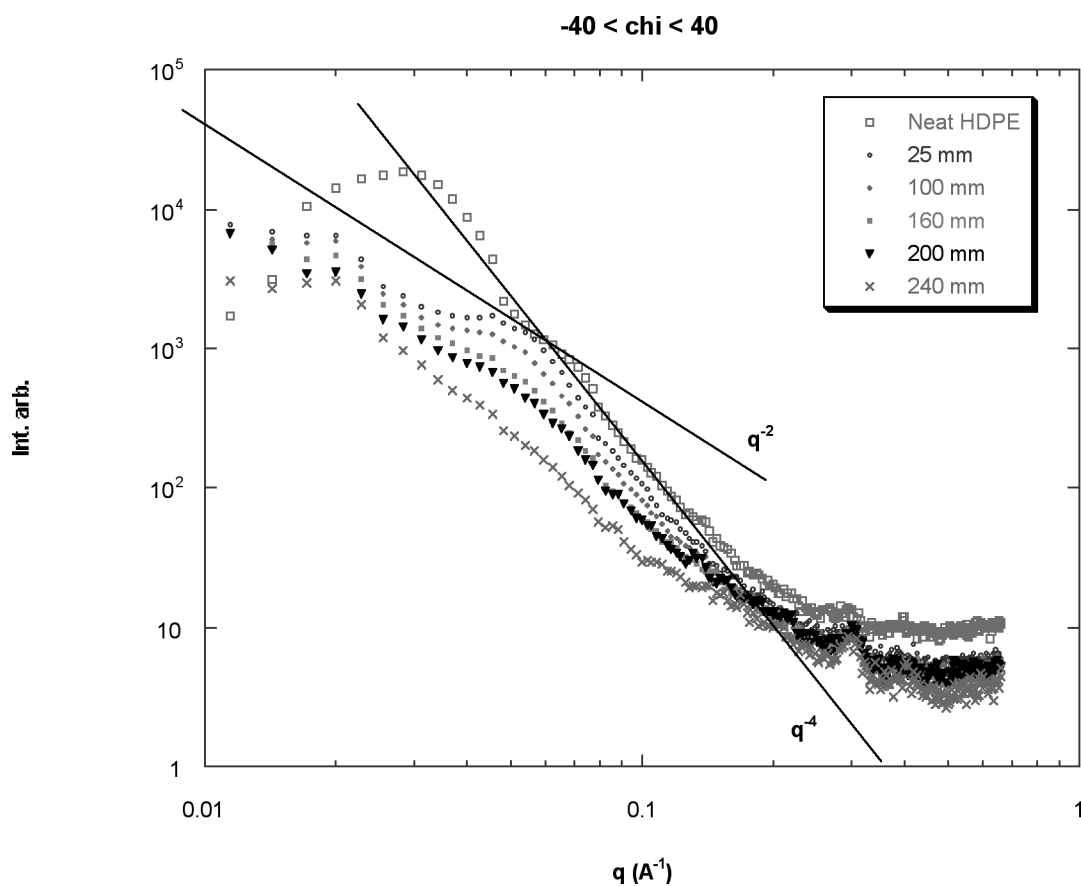


Figure III.2. Small angle X-ray scattering data from the UNM SAXS lab on bulk, drawn samples of PE. The samples are the same as used in the diffraction study. The values in the legend are the extensions, corresponding to draw ratios of 0, 0.2, 0.98, 3.94, 6.30, 7.87, and 9.45.

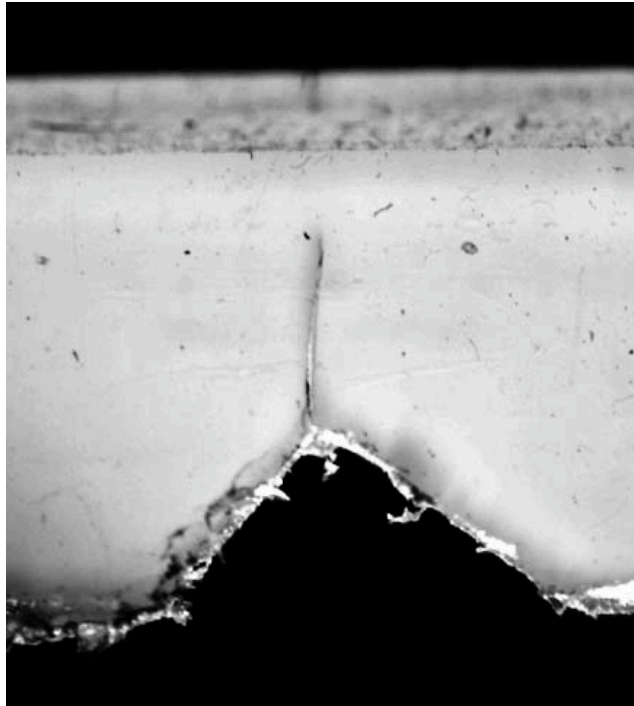


Figure III.3. Notched PE sample showing the crack which has grown from the tip of the notch under loading.

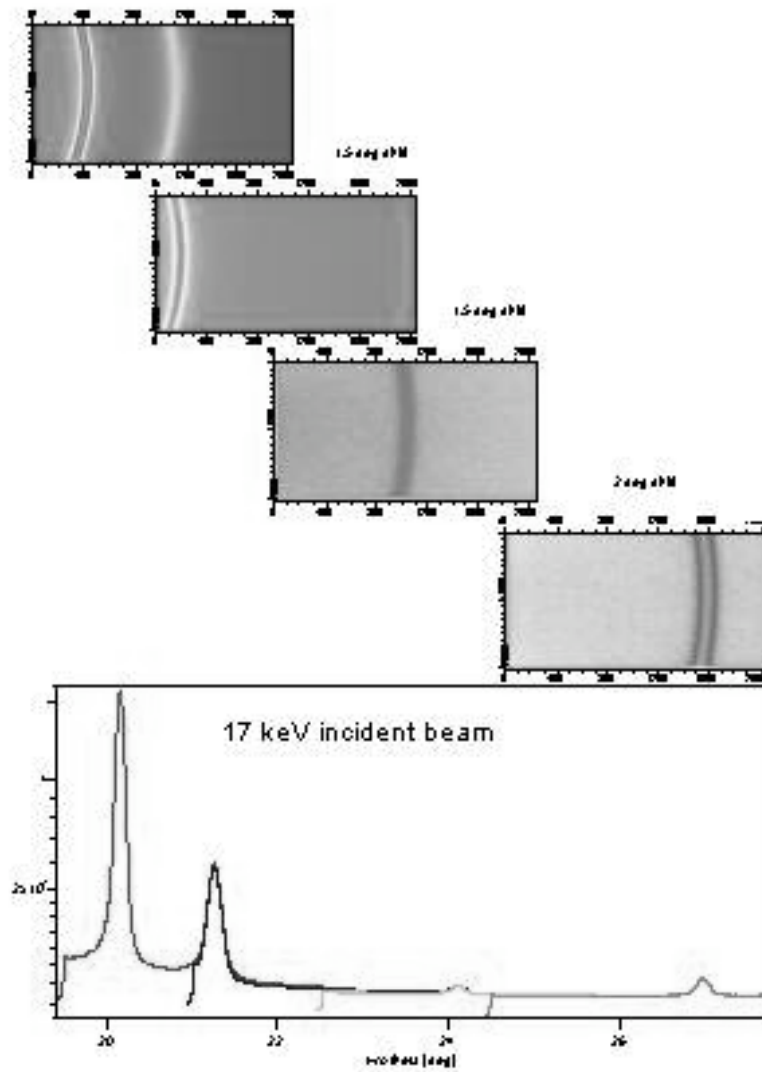


Figure III.4. X-ray diffraction data obtained from the notched PE sample near the crack tip taken with a 300 μm x 300 μm beam at the APS (without load). This same pattern was observed over the entire region around the crack tip as well as far away from the crack tip. However, the most sensitive region to the deformation occurs at higher q than obtained in this spectrum. Incident radiation is 17 KeV or 0.73 \AA .

III.3.2 Epoxy Studies

III.3.2.1 Small Angle X-ray Scattering

Small angle X-ray scattering was obtained for a notched epoxy sample on the pinhole camera at UNM with the help of Thomas Rieker. The sample was supplied by Prof. Ray Pearson (Lehigh University). To prepare the sample, a bulk sample had been originally notched and then loaded in 3 pt bend until shear yielding. A slice of the sample was obtained and then polished to a 1 mm thickness. The strain produced a permanent deformation, as could be easily seen in the birefringence from the sample. However, very little increase in scattering and no peaks were observed in the X-ray scattering analysis near the notch tip relative to far away from the notch. The pinhole camera produces a beam with a spot size of about 1 mm in diameter. The yield zone of the epoxy indicated by the birefringence pattern was substantially less than 1 mm. It is likely that the beam sampled nonyielded material as well as yielded material, and that a measurement with higher resolution is needed. Furthermore, the sample was not loaded during the measurement. Since X-ray scattering is sensitive to density variation, it may be that excess scattering will only be produced when the sample is under load. Further progress was hindered by the departure of Thomas Rieker from the UNM SAXS lab.

III.3.2.2 X-ray Tomography

Initial measurement and tomography analysis of a notched epoxy sample was performed at the APS over a 600 x 600 μm area. This particular sample was used because a detailed finite element analysis had been previously performed by B. Chambers which indicates the size and location of the deformation zone (See Figure III.5). Unfortunately, only measurements in the absence of load were obtained. Excellent image quality was obtained (Figure III.6), indicating that the method has promise. Striations in the sample are the effects of the finishing tool

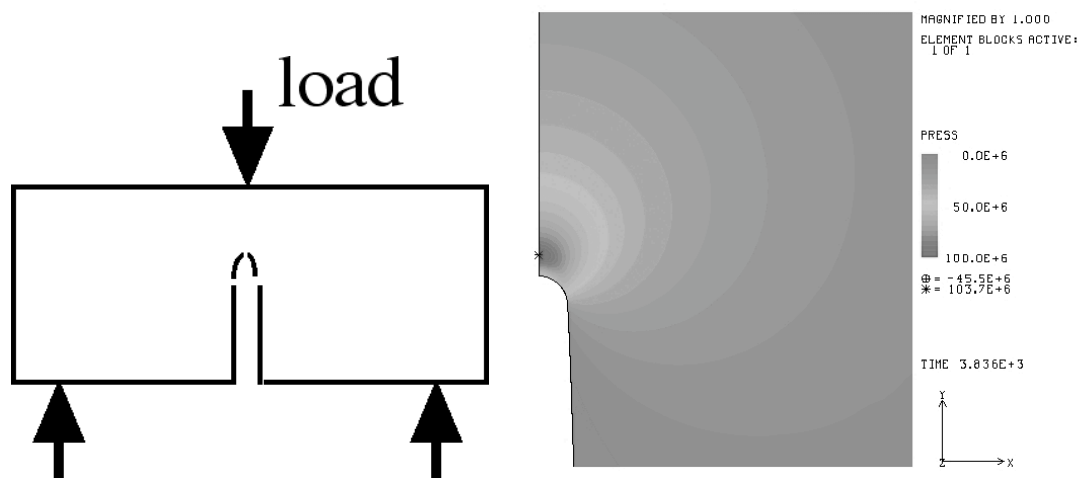


Figure III.5. FE analysis of notched epoxy sample. Deformation zone occurs ahead of the notch tip.

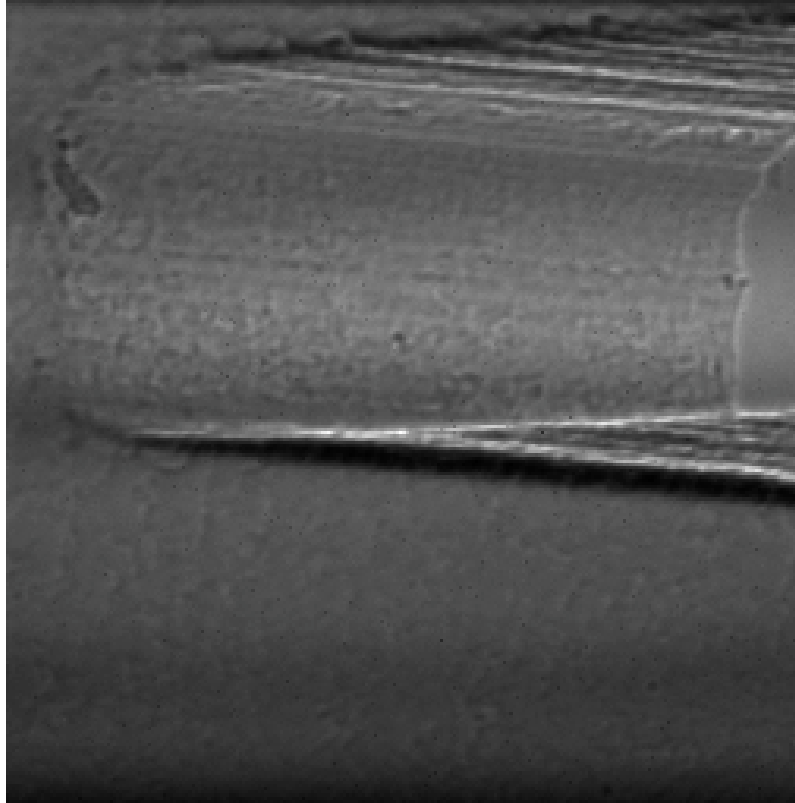


Figure III.6. High resolution computed X-ray tomography of the notched epoxy sample taken at the APS. The tip of the notch is at the right of the figure.

used to prepare the notch. In future work, X-ray tomography and X-ray scattering will be performed on this sample as a function of load until fracture and also for fatigued samples. Our goal is to determine the location of the deformation/initiation site for validation of the FE analysis.

III.4 Summary

Progress on the beamline capabilities at the APS was slower than anticipated, and thus we have not yet obtained the crucial data to evaluate the ultimate capabilities of this methodology. This requires ultra high resolution scattering, diffraction, or tomography data obtained under load for both notched epoxy and PE samples. However, the background work on bulk PE was entirely completed and the preliminary data to date from the APS suggests that measurement of strain fields near crack tips in semicrystalline polymers will be possible. Observing crack initiation in epoxy samples is more challenging, due to the smaller yield zone and the fact that catastrophic failure closely follows the initial deformation events. The outlook on this is still unclear, but should be answered in further work within the coming year.

IV. Interfacial Crack Growth Simulations

IV.1 Background

The objective of this computational study is to determine if an interfacial crack growth analysis, which uses a cohesive zone model based upon the molecular work of separation, can explain the observed experimental results. In particular, the analysis should be consistent with the data that describes how interfacial toughness varies with the strength of interfacial interactions (Figure II.18, measured using an ADBCS specimen with $\angle_{r=0.01 \text{ mm}}$ of -8°). This data indicates that:

- 1) There is a roughly linear relationship between G_c and G_o .
- 2) At the weakest level of interfacial interactions (i.e., 0% bromine-terminated SAM where $G_o \sim 0.05 \text{ J/m}^2$) the interfacial toughness exceeds the work of molecular separation by a factor of 40.
- 3) At the strongest level of interfacial interaction (i.e., 90% bromine-terminated SAM with an estimated G_o in the range of $1\text{-}2 \text{ J/m}^2$), the interfacial toughness exceeds the work of molecular separation by a factor of 20 to 40.

These observations suggest that G_c / G_o is at most weakly dependent on the strength of surface interactions and furthermore G_c / G_o has a value that is in the range of 20-40 for a $\angle_{r=0.01 \text{ mm}}$ of -8° .

IV.2 Approach

The rigid adherend, small-scale yielding simulations reported here ($\angle_{r=0.01 \text{ mm}} = -8^\circ$) employ the simplest material models possible with the aim of identifying the key ingredients needed in an analysis consistent with experimental observations. The analysis uses the same rate-independent cohesive zone model as used by Tvergaard and Hutchinson (1993). This model is based on a traction potential that depends on a scalar effective separation, and traction-separation relation defines the separation process (Figure IV.1). The

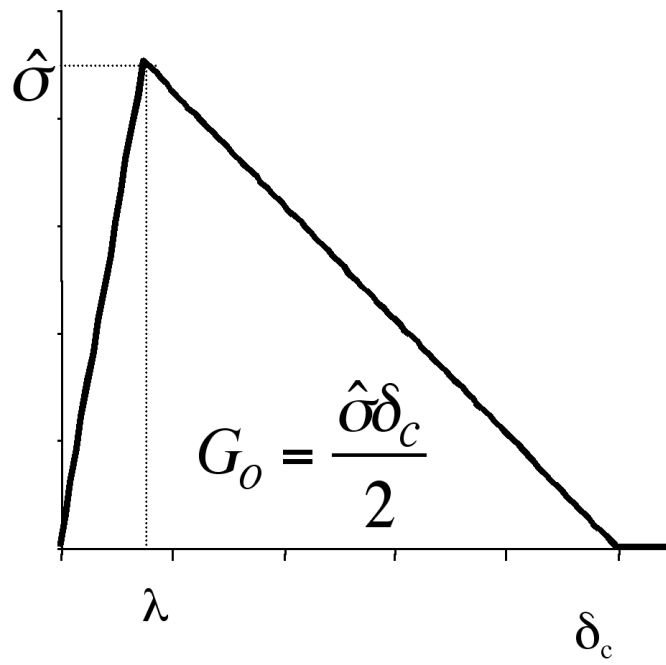


Figure IV.1 Traction-separation relation used to define the separation process in the interfacial crack growth simulations.

normal and tangential characteristic separation distances are assumed equal with a value of ℓ . The two key parameters in the traction-separation relation (TSS) model are the peak separation stress $\bar{\sigma}$ and the work of separation/unit area G_o (the area under the TSS curve). Since the shape of the TSS relation has been found to be relatively unimportant (Tvergaard and Hutchinson, 1993), a simple triangular relationship with a steep loading segment was used ($\ell=0.01$), and $G_o = 1/2 \bar{\sigma} \ell$. The characteristic separation distance ℓ (the only length scale in a small-scale yielding analysis) is assumed to be 1 nm; an order of magnitude estimate of the distance associated with bond failure. Note that when $\ell=1$ nm, G_o values of 0.05 J/m² and 1.0 J/m² (values associated with weak and strong interfacial interactions) imply $\bar{\sigma}$ values of 100 MPa and 1000 MPa, respectively.

IV.3 Model Inputs

The epoxy response in the highly strained region is not well understood, but is probably crucial to the success of the analysis. Figure IV.2 plots the measured compressive stress-strain relationship for the EPON 828/T-403 epoxy adhesive (test was terminated at a maximum nominal strain is 30%). As is often observed in a compression test of an unfilled epoxy, the stress-strain relation has an initial peak yield point, followed by softening. It is not known if this initial peak in the yield response persists when the epoxy is subjected to a high hydrostatic tensile component like that found at a crack tip. In the present work softening response is ignored, and yield strength, σ_y , is set equal to the 50 MPa plateau value attained after softening. Hence, $\bar{\sigma}/\sigma_y$ values in this study fall in the range of 2 to 20. This clearly presents a dilemma since a cohesive zone model predicts that a crack blunts and cannot advance when $\bar{\sigma}/\sigma_y > 3$; normal stress in front of a crack in a perfectly plastic material cannot exceed $3\sigma_y$ (Tvergaard and Hutchinson, 1992). This is the same dilemma that arises in the analysis of metal/ceramic interfaces, and has lead to considerable interest in strain gradient plasticity theories with an enhanced flow stress at the micron scale (Hutchinson, 1997). These theories are dislocation based, and are not applicable to polymers. Fortunately, there is another possibility for avoiding the $\bar{\sigma}/\sigma_y$ dilemma when the

material is a glassy polymer. After strain softening, the stress-strain curve of many polymers exhibits a local minimum in region of fairly constant stress (e.g., the plateau value in Figure IV.2 at ~30% strain) and then the curve stiffens at an progressively increasing rate until the stress is 2 to 3 times higher than the plateau value as the strain level approaches 100%, and furthermore, this type of stress-strain response has been observed in untoughened epoxies (Buckley et al., 2001). In the present study, a finite strain J-2 flow plasticity theory is used in conjunction with the stress-strain curve shown in Figure IV.2. The epoxy is modeled as elastic-perfectly plastic until the equivalent plastic strain exceeds 30%. The epoxy then hardens linearly with a flow stress of $3\sigma_y$ at 100% equivalent plastic strain. This is a rather simplistic model for a glassy epoxy, but captures in at least a crude way the desired hardening response at large strain (Landis et al., 2000). It is worth noting that recent molecular dynamics simulations for an highly cross-linked polymer network confined between solid surfaces and subjected to a tensile loading generates a similar stress-strain curve, and that the simulation indicates that interfacial failure occurs in the region of rapid hardening as the polymer strands are pulled taut (Stevens, 2001).

IV.4 Crack Growth Simulations

IV.4.1 Small Scale Yielding

The small-scale yielding crack growth simulations were performed using the mesh shown in Figure IV.3. The mesh has a 1-mm (10^6 nm) radius with boundary displacements defined by the bimaterial elastic asymptotic solution for a rigid upper material with an applied mode mixity equal to that of ADCBS specimens tested in this study ($\varphi_{r=0.01\text{ mm}} = -8^\circ$). The mesh incorporates a 500-nm long region of 1-nm elements at the initial crack tip to allow up to 0.5 μm of crack growth. JAS3D implements the traction-separation relation via the contact algorithm, and reduced integration, 8-noded hex elements are used to model the bulk material. Plane strain results were obtained by suitably constraining the

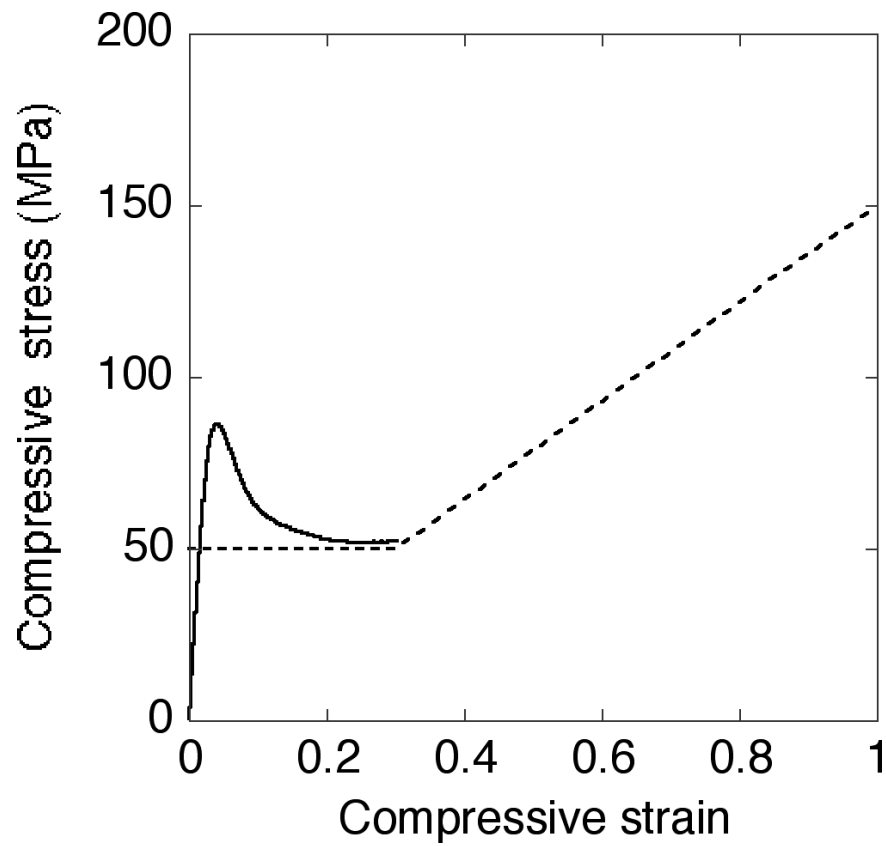


Figure IV.2 Compressive stress-strain relationship for the EPON 828/T-403 epoxy adhesive (solid curve) along with model used in calculations (dotted curve).

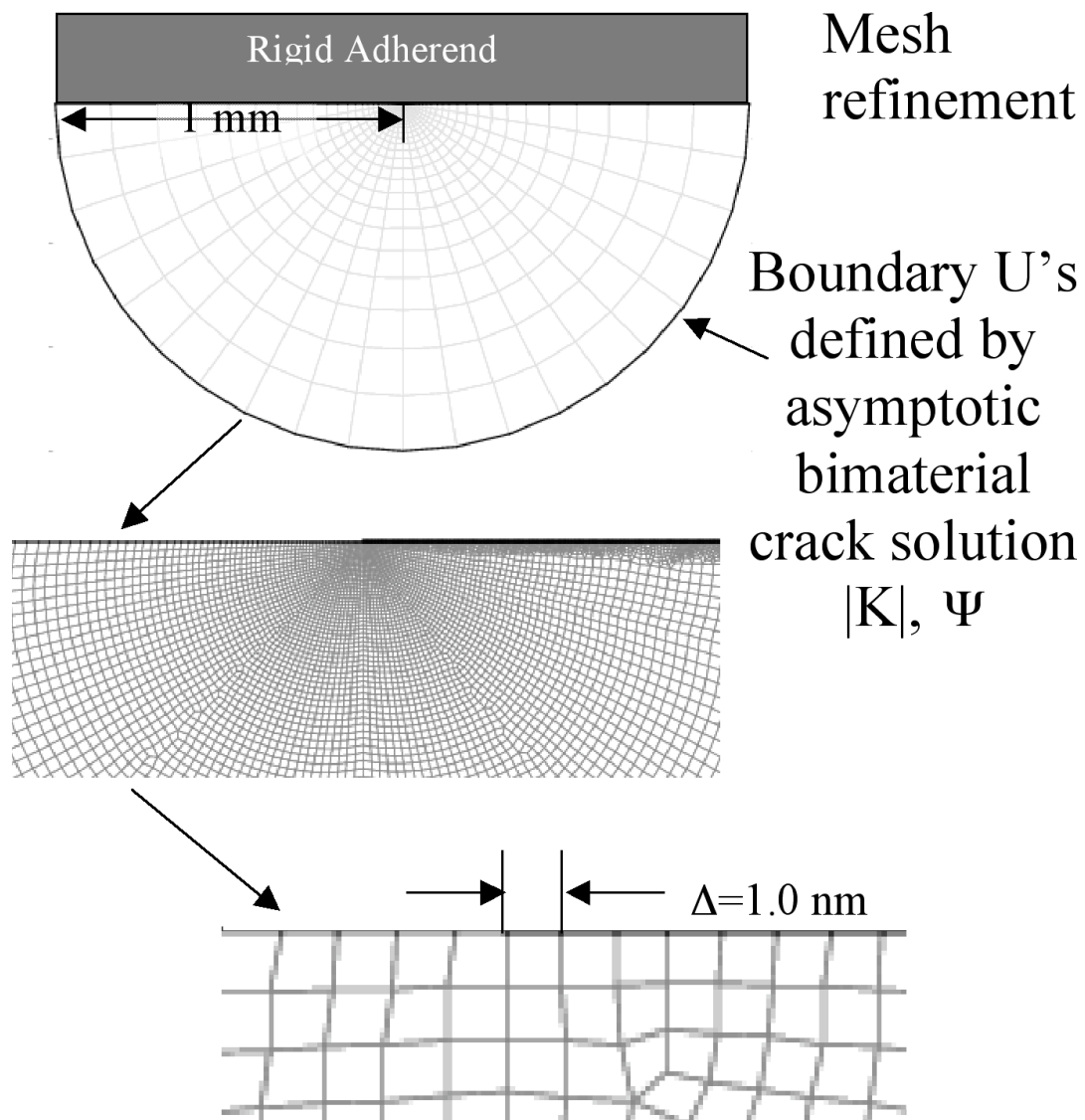


Figure IV.3 Finite element mesh used in the small-scale yielding crack growth simulations.

front and back surfaces of the hex elements. Calculated results should be independent element size provided that the mesh is capable of resolving the cohesive zone. Convergence was investigated by varying the ratio of critical separation distance ℓ_c (the only length scale in the small-scale yielding problem) to the element size at the crack tip (ℓ). Figure IV.4 shows that ℓ_c/ℓ needs to be greater than 4 for a convergent solution, and all results reported here are for $\ell_c/\ell=8$. Interestingly this ℓ_c/ℓ is much greater than that typically reported in cohesive zone simulations (e.g. in Hutchinson and Suo (1992) $\ell_c/\ell=0.1$). Even though lower ℓ_c/ℓ values are adequate to resolve the size of the yield zone, the higher ℓ_c/ℓ is needed to resolve blunting in a material with low hardening.

IV.4.2 Strain Energy Release Rate

Figure IV.5 plots the calculated energy release rate to propagate an interfacial crack G^r (normalized by G_0) vs. crack extension (normalized by a distance ℓ) as a function of $\tilde{\ell}/\ell_y$. Subcritical crack growth begins when the applied energy release rate G equals G_0 . A steady state G , G_{ss} is realized when $\tilde{\ell}/\ell_y < 2.7$, and $G_{ss}/G_0=7$ when $\tilde{\ell}/\ell_y=2.7$. When $\tilde{\ell}/\ell_y > 3.0$, crack extension no longer depends on $\tilde{\ell}/\ell_y$. Crack extension is governed by the highly localized region of elevated stress associated with strain stiffening at the crack tip, not by yielding. Crack growth is stable, and arbitrarily large G^r/G_0 can be attained as $\ell a/\ell_c$ increases (i.e., there is no G_{ss}). Based upon dimensional considerations for small-scale yielding,

$$G^r = G_0 f\left(\frac{\ell a}{\ell_c}, \nu_r = \nu_c, \frac{\ell}{\ell_y}, \nu, \frac{\ell_y}{E}, \nu_b, \ell_b, \frac{H}{\ell_y}\right) \quad \text{where} \quad G_0 = \frac{\ell \ell_c}{2} \quad (19)$$

where E is Young's modulus, ν is Poisson's ratio, ℓ_b is the strain level where strain-stiffening commences, and H is the stiffening modulus. When $\tilde{\ell}/\ell_y > 3.0$, the calculations indicate that f is independent of $\tilde{\ell}/\ell_y$ and since all other material

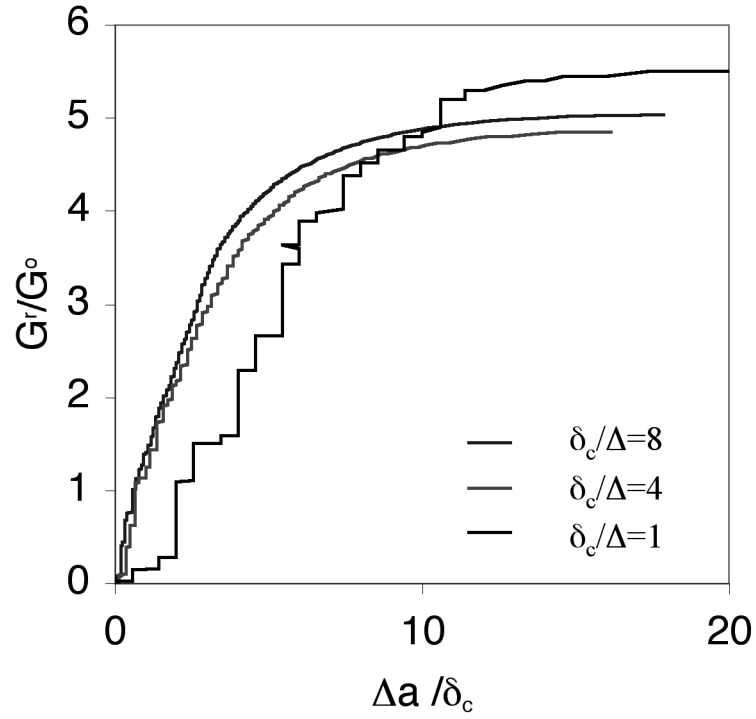


Figure IV.4 Convergence study to determine the minimum ratio of critical characteristic separation/element size needed to resolve cohesive zone ($\sigma_y/\sigma_c=2.5$).

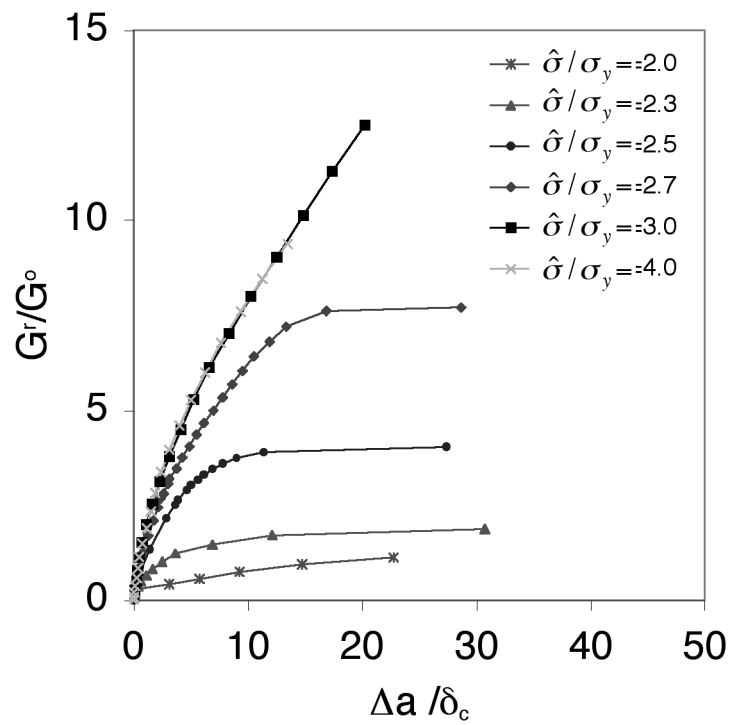


Figure IV.5 Calculated energy release rate to propagate an interfacial crack vs. crack extension as a function of $\hat{\sigma} / \sigma_y$.

parameters are constant, $G^r = G_o f(\Delta a / \Delta_c)$. This result is consistent with experimental observation in the sense that G^r is directly proportional to G_o , and G^r / G_o can be large. The analysis is deficient in that no steady-state G is predicted when $\Delta / \Delta_y > 3.0$. This deficiency is associated with the choice of linear strain stiffening and the lack of an ultimate rupture strain. Linear strain stiffening is in fact an oversimplification, since in reality stiffening occurs with a progressively increasing modulus; the capacity for plastic deformation is “used up” as the epoxy’s ultimate rupture strain is approached. For this reason, simulations that incorporate such strain stiffening are planned in future work.

IV.5 Summary

The fracture toughness of SAM-coated aluminum/epoxy interfaces with a range of well-defined interfacial interactions has been measured with an asymmetrical double cantilever beam sandwich (ADCBS) specimen. Interfacial interactions were varied using self-assembled monolayers containing mixtures of molecules with different terminal groups. The measured interfacial toughness increased by about a factor of 20 as the strength of interfacial interactions was increased. In the complementary modeling effort, interfacial crack growth simulations have been performed using 1) a cohesive zone separation criterion based upon the molecular work of separation and a critical separation distance of 1 nm and 2) large-strain constitutive models for the deformation within the highly deformed crack-tip process zone. The inclusion of epoxy strain stiffening at large strains in the analysis generates a high interfacial toughness to the molecular work of separation ratio that is independent of the strength of the surface interactions, a result that is consistent with experimental observation.

V. Acknowledgments

The authors wish to thank John Emerson from Sandia National Laboratories, Albuquerque, NM for many helpful technical discussions. We are grateful to Prof. David F. Bahr from Washington State University for helping develop then depositing stressed overlayers onto our epoxy samples. We also thank P.J. Klein and M.E. Stavig developing the fabrication and testing techniques for the ADCBS and TBNS specimens We extend a special thanks to Christy Woodcock and Kirsten Schafer from Washington State University for their technical assistance and Yvete Toivola from the University of Minnesota for performing ATR spectroscopy. The authors also gratefully acknowledge the support of U.S. DOE Contract DE-AC04-94AL85000.

VI. Tables

Table II.1 Average hardness, yield strength, stress, and fracture energies from delaminations in 11.8 μm thick Epon 828/T403.

h (μm)	H (MPa)	σ_{ys} (MPa)	σ_{rb} (MPa)	$\sigma(\sigma)$ (J/m ²)	σ	σ_I (J/m ²)
11.8	250	115	141	3.6 \pm 1.1	-37	2.7 \pm 0.1

Table II.2 Average film thickness, blister half-widths, delamination stresses, residual stresses, and fracture energies from telephone cord blisters in 24, 164, and 615 nm thick Epon 828/T403 films.

Thickness		b (μm)	Stress		Fracture Energy		
h_{ep} (nm)	h_W (nm)		σ_b (GPa)	σ_r (GPa)	$\sigma(\sigma)$ (J/m ²)	σ	σ_I (J/m ²)
24	220	4.4	1.0	-2.1	1.7 \pm 0.1	-75	0.6 \pm 0.1
164	220	6.5	0.3	-1.3	1.7 \pm 0.1	-86	0.4 \pm 0.1
615	220	6.0	0.3	-0.6	1.5 \pm 0.1	-62	0.8 \pm 0.1

Table II.3 Average film thickness, blister radius, delamination stress, residual stress, and fracture energies from indentation-induced circular blisters in 164 nm thick Epon 828/T403.

Thickness		a (μm)	Stress		Fracture Energy		
h_{ep} (nm)	h_W (nm)		σ_b (GPa)	σ_r (GPa)	$\sigma(\sigma)$ (J/m ²)	σ	σ_I (J/m ²)
164	220	5.3	0.6	-1.1	0.9 \pm 0.3	-61	0.5 \pm 0.1

Table II.4 Film thickness, properties and crack tip opening angles used to calculate fracture energies in 164 and 615 nm thick Epon 828/T403 films.

Blister Morphology	Thickness	Properties			Fracture Energies	
	h_{ep} (nm)	E_{ep} (GPa)	σ_{ys} (MPa)	CTOA (radians)	J_{ss} (J/m ²)	J_o (J/m ²)
circular	164	4.35	115	0.10	0.9 \pm 0.3	0.4 \pm 0.1
telephone	615	4.35	115	0.09	1.5 \pm 0.1	0.8 \pm 0.1

VII. References

Agrawal, R. K., Drzal, L. T. (1995a) Adhesion mechanisms of polyurethanes to glass surfaces I. Structure-property relationships in polyurethanes and their effects on adhesion to glass, *Journal of Adhesion* **54**, 79.

Agrawal, R. K., Drzal, L. T. (1995b) Adhesion mechanisms of polyurethanes to glass surfaces II. Phase separation in polyurethanes and their effects on adhesion to glass, *Journal of Adhesion Science and Technology* **9**, 1381-1400.

Akisanya, A. R. and N. A. Fleck (1992). Brittle fracture of adhesive joints, *International Journal of Fracture* **58**, 93-114.

Bagchi, A., Evans, A. G. (1996) Measurements of the debond energy for thin metallization lines on dielectrics, *Thin Solid Films* **286**, 203-212.

Bagchi, A., Lucas, G. E., Suo, Z., Evans, A. G. (1994) A new procedure for measuring the decohesion energy for thin ductile films on substrates, *Journal of Materials Research* **9**, 1734-1741.

Bao, G., S. Ho, et al. (1992) The role of material orthotropy in fracture specimens for composites, *International Journal of Solids and Structures* **29**, 1105-1116.

Buckley, C. P., J. Harding, et al. (2001) Deformation of thermosetting resins at impact rates of strain. Part I: Experimental study, *Journal of the Mechanics and Physics of Solids* **49**, 1517-1538.

Bulter, M. F., Donald, A. M., Bras, W., Mant, G. R., Derbyshire, G. E., Ryan, A. J. (1995) A real-time simultaneous small- and wide-angle x-ray scattering study of in-situ deformation of isotropic polyethylene, *Macromolecules* **28**, 6383-6393.

Emerson, J. A., Reedy, E. D., Adams, D. P., Moody, N. R., (2003) Process-based quality tools to verify cleaning and surface preparation, *Sandia Report*.

Evans, A. G., Hutchinson, J. W. (1984). On the mechanics of delamination and spalling in compressed films, *International Journal of Solids and Structures* **20**, 455-466.

Evans, A. G., Ruhle, M., Dalgleish, B. J., Charalambides, P. G. (1990) The fracture energy of bimaterial interfaces. In: *Metal-Ceramic Interfaces* (edited by Ruhle, M., Evans, A. G., Ashby, M. F., Hirth, J. P.) Pergamon Press, Oxford, 345-364.

Hutchinson, J. W., Suo, Z. (1992) Mixed mode cracking in layered materials, *Advances in Applied Mechanics*, (edited by Hutchinson, J. W., Wu, T. Y.) Academic Press Inc., New York. NY, **29**, 63-191.

Hutchinson, J. W. (1997) Linking scales in fracture mechanics, *Advances in Fracture Research* (edited by Karimhaloo, B. L., Mai, Y.-W., Ripley, M. I., Ritchie, R. O.) Pergamon Press, Oxford, 1-14.

Kent, M. S., Reedy, E. D., Stevens, M. J. (2000) Molecular-to-continuum fracture analysis of thermosetting polymer/solid interfaces, *Sandia Report SAND2000-0026*.

Kent, M. S., H. Yim, et al. (2001) Use of self-assembled monolayers at variable coverage to control interface bonding in a model study of interfacial fracture: pure shear loading, *Journal of Adhesion* **75**, 267-298.

Kriese, M. D., Moody, N. R., Gerberich, W. W. (1998) Effects of annealing and interlayers on the adhesion energy of copper thin films to SiO₂/Si substrates, *Acta materialia* **46**, 6623-6630.

Kriese, M. D., Gerberich, W. W., Moody, N. R. (1999) Indentation of superlayers as a quantitative probe of thin-film interfacial adhesion energy I. Mechanics of interfacial delamination, *Journal of Materials Research* **14**, 3007-3018.

Kuhl, A. and J. Qu (2000) A technique to measure interfacial toughness over a range of phase angles, *Journal of Electronic Packaging* **122**, 147-151.

Landis, C. M., T. Pardoen, et al. (2000) Crack velocity dependent toughness in rate dependent materials, *Mechanics of Materials* **32**, 663-678.

Liang, Y.-M. and K. M. Liechti (1995) Toughening mechanisms in mixed-mode interfacial fracture, *International Journal of Solids and Structures* **32**, 957-978.

Liechti, K. M. and Y. S. Chai (1992) Asymmetric shielding in interfacial fracture under in-plane shear, *Journal of Applied Mechanics* **59**, 295-304.

Lucas, B. N., Rosenmayer, C. T., Oliver, W. C. (1998a) Mechanical characterization of sub-micron polytetrafluoro ethylene (PTFE) thin films, *Thin Films-Stresses and Mechanical Properties VII* (edited by Cammarata, R. C., Nastasi, M., Busso, E. P., Oliver, W. C.) Materials Research Society, Pittsburgh, PA, **505**, 97-102.

Lucas, B. N., Oliver, W. C., Swindeman, J. E. (1998b) The dynamics of frequency-specific, depth-sensing indentation testing, *Fundamentals of Nanoindentation and Nanotribology* (edited by Moody, N. R., Gerberich, W. W., Burnham, N., Baker, S. P.) Materials Research Society, Pittsburgh, PA, **522**, 3-14.

Marsh, D. M. (1963) Plastic flow in glass, *Proceedings of the Royal Society A* **279**, 420-435.

Marshall, D. B., Evans, A. G. (1984) Measurement of adherence of residually stressed thin films by indentation mechanics of interface delamination, *Journal of Applied Physics* **56**, 2632-2638.

Moody, N. R., Bahr, D. F., Kent, M. S., Emerson, J. A., Reedy, E. D. (2001) Adhesive failure of thin epoxy films on aluminized substrates, *Fundamentals of*

Nanoindentation and Nanotribology II (edited by Cook, R. F., Baker, S. P., Corcoran, S. G., Moody, N. R.) Materials Research Society, Pittsburgh, PA, **649**, Q6.3.1-6.

Moody, N. R., Yang, N., Adams, D. P., Cordill, M. J., Bahr, D. F. (2002) Film thickness effects on interfacial failure of epoxy bonds, *Polymer Interfaces and Thin Films* (edited by Karim, A., Frank, C. W., Russell, T. P., Nealy, P. F.) Materials Research Society, Pittsburgh, PA, **710**, DD10.6.1-6.

Rice, J. R., Drugan, W. J., Sham, T.-L. (1980) Elastic-plastic analysis of growing cracks, *Fracture Mechanics: Twelfth Conference*, ASTM STP 700, American Society for Testing and Materials, Philadelphia, PA, 189-221.

Rice, J. R. (1988) Elastic fracture mechanics concepts for interfacial cracks, *Journal of Applied Mechanics* **55**, 98-103.

Ritter, J. E., Lardner, T. J., Rosenfeld, L., Lin, M. R. (1989) Measurement of adhesion of thin polymer coatings by indentation, *Journal of Applied Physics* **66**, 3626-3634.

Rosenfeld, L. G., Ritter, J. E., Lardner, T. J., Lin, M. R. (1990) Use of the microindentation technique for determining interfacial fracture energy, *Journal of Applied Physics* **67**, 3291-3296.

Stevens, M. J. (2001) Interfacial fracture between highly cross-linked polymer networks and a solid surface: effect of interfacial bond density, *Macromolecules* **34**, 2710-2718.

Strojny, A., Moody, N. R., Emerson, J. A., Gerberich, W. W. (2000) Interfacial Fracture of Thin Polymer Films on Aluminum, *Polymer Systems*, (edited by Anastasiadis, S. H., Karim, A., Ferguson, G. S.) Materials Research Society, Pittsburgh, PA, **629**, F5.13.1-6.

Suo, Z., Hutchinson, J. W. (1989) Sandwich test specimen for measuring interface crack toughness, *Material Science and Engineering* **A107**, 135-143.

Swadener, J. G., Liechti, K. M., de Lozanne, A. L. (1999) The intrinsic toughness and adhesion mechanisms of a glass/epoxy interface, *Journal of the Mechanics and Physics of Solids* **47**, 223-258.

Thouless, M. D. (1988) Decohesion of films with axisymmetric geometries, *Acta Metallurgica* **36**, 3131-3135.

Tvergaard, V. and Hutchinson, J. W. (1992) The relation between crack growth resistance and fracture process parameters in elasti -plastic solids, *Journal of the Mechanics and Physics of Solids* **40**, 1377-1397.

Tvergaard, V., Hutchinson, J. W. (1993) The influence of plasticity on mixed mode interface toughness, *Journal of the Mechanics and Physics of Solids* **41**, 1119-1135.

Volinsky, A. A., Gerberich, W. W. (1999) Acoustic emission analysis of fracture events in Cu films with W overlayers, *Materials Reliability in Microelectronics IX* (edited by Volkert, C. A., Verbruggen, A. H., Brown, D.) Materials Research Society, Pittsburgh, PA, **563**, 275-284.

Volinsky, A., Tymiak, N. I., Kriese, M. D., Gerberich, W. W., Hutchinson, J. W. (1999) Quantitative modeling and measurement of copper thin film adhesion, *Fracture and Ductile vs Brittle Behavior-Theory, Modeling, and Experiment* (edited by Beltz, G. E., Blumberg-Selinger, R. L., Marder, M. P., Kim, K-S.) Materials Research Society, Pittsburgh, PA, **539**, 277-290.

Wei, Y., Hutchinson, J. W. (1998) Interface strength, work of adhesion and plasticity in the peel test, *International Journal of Fracture* **93**, 315-333.

Zhuk, A. V., Evans, A. G., Hutchinson, J. W., Whitesides, G. M. (1998) The adhesion energy between polymer thin films and self-assembled monolayers, *Journal of Materials Research* **13**, 3555-3564.

Distribution List

3	MS 9018	Central Technical Files, 8945-1
1	MS 0899	Technical Library, 9616
1	MS 9021	Classification Office, 8511 / Technical Library, MS 0899, 9616 DOE/OSTI via URL
5	MS9404	Neville Moody, 8725
5	MS0893	Earl D. Reedy, Jr., 9123
5	MS1411	Michael S. Kent, 1851
1	MS9404	John R. Garcia, 8725
1	MS0889	Richard Salzbrenner, 1835
1	MS0893	Rebecca Brannon, 893
1	MS9401	Jill Hruby, 8702